MASTERARBEIT | MASTER'S THESIS

Titel | Title

Detachment versus strike-slip ductile shearing in the Nordrahmenzone of the Tauern Window

verfasst von | submitted by

Jakob Brunner BSc

angestrebter akademischer Grad | in partial fulfilment of the requirements for the degree of

Master of Science (MSc)

Wien | Vienna, 2025

Studienkennzahl lt. Studienblatt | Degree programme code as it appears on the student record sheet:	UA 066 815
Studienrichtung lt. Studienblatt | Degree programme as it appears on the student record sheet:	Masterstudium Erdwissenschaften
Betreut von | Supervisor:	Univ.-Prof. Mag. Dr. Bernhard Grasemann

Acknowledgment of the usage of AI

I acknowledge the use of the AI tool ChatGPT (https://chatgpt.com/) to help me in the refinement of my academic language and to generally identify improvements in the writing style. I confirm that I have read and understood the AI usage guidelines from the University of Vienna and that this thesis complies with them.

I Acknowledgements

During my studies I met a lot of people that played a part on my road to becoming a Geologist.

First and foremost, I want to thank my supervisor Bernhard Grasemann from the University of Vienna for his support and advice during the realization of this thesis. Bernhard, thank you for giving me the chance to work on this topic and for giving me the space and time to work on my own, but on the other hand also being there whenever I needed someone to discuss my work. Thank you also for your enthusiasm about my work, that always helped me to carry on, even in times when the work was progressing slowly and the motivation was low.

I also want to thank Gerd Rantitsch from the University of Leoben for giving me the opportunity to carry out RSCM measurements myself at the University of Leoben and for analysing the data. Special thanks also to Michel Bestmann from the University of Vienna for his help with optical cathodoluminescence and discussing microstructural observations.

I would like to further thank all the people of the Structural Processes Group of the Institute of Geology at the University of Vienna for making the working environment great and for all the critical questions and suggestions during my seminar talks.

Also, thanks to my parents and grandparents for always supporting me in every way possible, financially as well as mentally. Special thanks also to my grandmother Erika, who with her passion for collecting rocks and minerals most definitely fuelled my fascination with geology early on in my childhood.

Many thanks go out to my fellow students Michael, Aubert, Juliana, Marco, Basti, Thomas, Sophia *2, Lukas, Nils, Fiona*2 and all others for the countless hours studying, discussing, complaining about things and for all the nice evenings we spent together.

II Abstract

The Tauern Window in the Eastern Alps represents one of the most prominent tectonic windows. Many previous studies have established a widespread understanding of the processes contributing to the exhumation of the Tauern Window including shortening, extrusion and extension. This work presents new structural field data, microstructural observations and Raman micro spectroscopy of carbonaceous materials (RSCM) from an area within the Nordrahmenzone in the northeastern Tauern Window. These data show 4 deformation phases, which partly overlap during N-S shortening and W-E extension and continuous exhumation of the Penninic Unit below the Lower Austroalpine Unit: The first phase represents mylonitization that is associated with the newly described *Schuhflicker Detachment* that predates the activity along the Katschberg Normal Fault. RSCM data show that this detachment was active at a peak temperature of around 350-400°C. The mylonites belonging to the detachment have been folded in a second phase into regional scale upright to S-vergent folds. Depending on the fold limbs, the sub- vertically dipping mylonites show apparent sinistral and dextral strike slip shear senses proving that mylonitization predates folding. A concurrent third phase of deformation led to vertical flattening before the top to E deformation transferred to the Katschberg Normal Fault at around 21Ma. The fourth phase of deformation indicate continuous W-E extension along brittle-ductile to brittle N-S striking high angle faults.

The study also provides an important result for the Salzach Valley–Ennstal–Mariazell–Puchberg (SEMP) fault at the northern margin of the Tauern Window: Upright fold limbs of mylonitic marbles at the northern margin of the Tauern Window have been previously mistaken to be associated with the sinistral SEMP fault. However, these marble mylonites belong to our first phase of deformation and are folded by the second phase in upright folds. Therefore, the SEMP fault lacks a ductile component and is exclusively a brittle strike-slip fault localizing in clay gouges at the northern border of the Penninic Unit.

III Zusammenfassung

Das Tauernfenster in den Ostalpen ist eines der markantesten tektonischen Fenster. Viele frühere Studien haben zu einem umfassenden Verständnis über die Prozesse, die zur Exhumation des Tauernfensters beigetragen haben, geführt, darunter Verkürzung, Extrusion und Extension. Diese Arbeit präsentiert neue strukturgeologische Geländedaten, mikrostrukturelle Beobachtungen und Raman Mikro Spektroskopie an kohlenstoffhaltigen Materialien (RSCM) aus einem Gebiet in der Nordrahmenzone, im nordöstlichen Tauernfenster. Diese Daten zeigen 4, teilweise überlappende, Deformationsphasen während N-S Verkürzung, W-O Extension und kontinuierlicher Exhumation der Penninischen Einheiten unter der Unterostalpinen Einheit. Die erste Phase stellt Mylonitisierung im Zusammenhang mit dem neu beschriebenen *Schuhflicker Detachment* dar, dessen Aktivität der Aktivität an der Katschberg Abschiebung voran geht. Die RSCM-Daten zeigen, dass dieses Detachment bei einer maximalen Temperatur von rund 350-400°C aktiv war. Die zum Detachment gehörenden Mylonite wurden in einer zweiten Phase zu großräumigen, aufrechten bis süd- vergenten Falten verfaltet. Abhängig vom Faltenschenkel zeigen die sub- vertikal einfallenden Mylonite dextrale oder sinistrale Schersinne, die zeigen, dass die Mylonitisierung vor der Faltung stattgefunden hat. Eine zeitgleiche dritte Deformationsphase führte zu vertikaler Verkürzung bevor die Top E- Deformation vor Rund 21Ma auf die Katschberg Abschiebung über ging. Die vierte Deformationsphase zeigt kontinuierliche W-O Extension an spröd- duktilen bis spröden, N-S streichenden Abschiebungen.

Diese Studie liefert zudem ein wichtiges Ergebnis für die Salzachtal- Ennstal- Mariazell Puchberg (SEMP) Störung am Nordrand des Tauernfensters. Die aufrechten Faltenschenkel mylonitischer Marmore wurden früher fälschlicherweise mit der sinistralen SEMP in Verbindung gebracht. Diese Marmore gehören jedoch zu unserer ersten Deformationsphase und sind von der zweiten Deformationsphase in aufrechte Falten verfaltet worden. Daher fehlt der SEMP eine duktile Komponente und sie stellt eine vollkommen spröde Blattverschiebung dar, die an der nördlichen Grenze der Penninischen Einheit in Ton- Gouges lokalisiert.

IV List of abbreviations

D	deformation phase
s	schistosity plane
l	lineation
fa	fold axis
axpl	fold axial plane
saxpl	axial plane cleavage
SPO	shape preferred orientation
CPO	crystallographic preferred orientation
XPL	crossed polarized light
PPL	planar polarized light
CL	cathodoluminescence
Qz	quartz
Fsp	feldspar
Wm	white mica
Cal	calcite
Dol	dolomite
Gr	graphite
Pyr	pyrite
KSZS	Katschberg Shear Zone System
BNF	Brenner Normal Fault
KNF	Katschberg Normal Fault
SEMP	Salzach Valley- Ennstal- Mariazell- Puchberg Fault

Contents

1 Introduction

The Tauern Window in the Eastern Alps is one of the most prominent tectonic windows, which formed as a result of the subduction of the Alpine Tethys followed by the collision between the Adriatic and European continents in the Eocene. It exposes Penninic and Subpenninic Units derived from the Alpine Tethys and the European continent below Austroalpine Units derived from the Adriatic continent (Schmid et al., 2013 and references therein). Generally, it is considered, that the exhumation in the Tauern Window is localized at the Brenner Normal Fault (BNF) at its western margin (e.g. Fügenschuh et al., 1997; Rosenberg & Garcia, 2011) and the Katschberg Normal Fault (KNF) at the eastern margin (e.g. Genser & Neubauer, 1989; Wolff et al., 2024). The deformation at the Brenner Normal Fault started at around 20 Ma (Fügenschuh et al., 1997), the deformation at the Katschberg Normal Fault is dated to be slightly older starting at 21.1 Ma (Wolff et al., 2024). However, the exhumation of eclogite bearing units in the Tauern Window started 10Ma earlier than the BNF and the KNF (e.g. Glodny et al., 2005; Kurz et al., 2008). In this work we demonstrate that the exhumation in the Eastern Tauern Window is coeval with the decompression of the eclogites and deformation is localized in pervasive mylonites (Klammkalk) in the Nordrahmenzone overprinted by a strong N-S shortening component during W-E extension. Our findings also suggest that the Klammkalk mylonites are not the ductile part of the SEMP fault (Frost et al., 2011; Wang & Neubauer, 1998) but rather the upright folded mylonites of a major top to E detachment.

This work investigates several N-S traverses east and west of the Großarl Valley around Mt. Saukarkopf and Mt. Schuhflicker respectively. Structural fieldwork, as well as observations made by optical microscopy and optical cathodoluminescence are used to constrain the tectonic history of the Nordrahmenzone and its border with the Lower Austroalpine. Raman micro spectroscopy of carbonaceous materials was used to determine the peak metamorphic temperatures at around 350-400°C. A new geological map of the area around Mt. Saukarkopf inferred from field data and old maps (Peer & Zimmer, 1977) is presented. Based on the new data from this study as well as existing geochronological data a new model for the tectonic evolution of the study area and its implications on the regional tectonic evolution of the border of the Tauern Window with the Austroalpine Superunit is presented.

2 Geological Overview

The Eastern Alps (Figure 1) are a European mountain range belonging to the Alpine- Himalayan Orogenic belt. They have been formed due to the collision of the Adriatic microplate with the Eurasian plate in the Cenozoic. The major tectonic units of the Eastern Alps are defined by their paleogeographic origin from the European continent, the Penninic oceans, the Neo-Tethys ocean and the Adriatic continent (Froitzheim et al., 2008; Schmid et al., 2004). During the

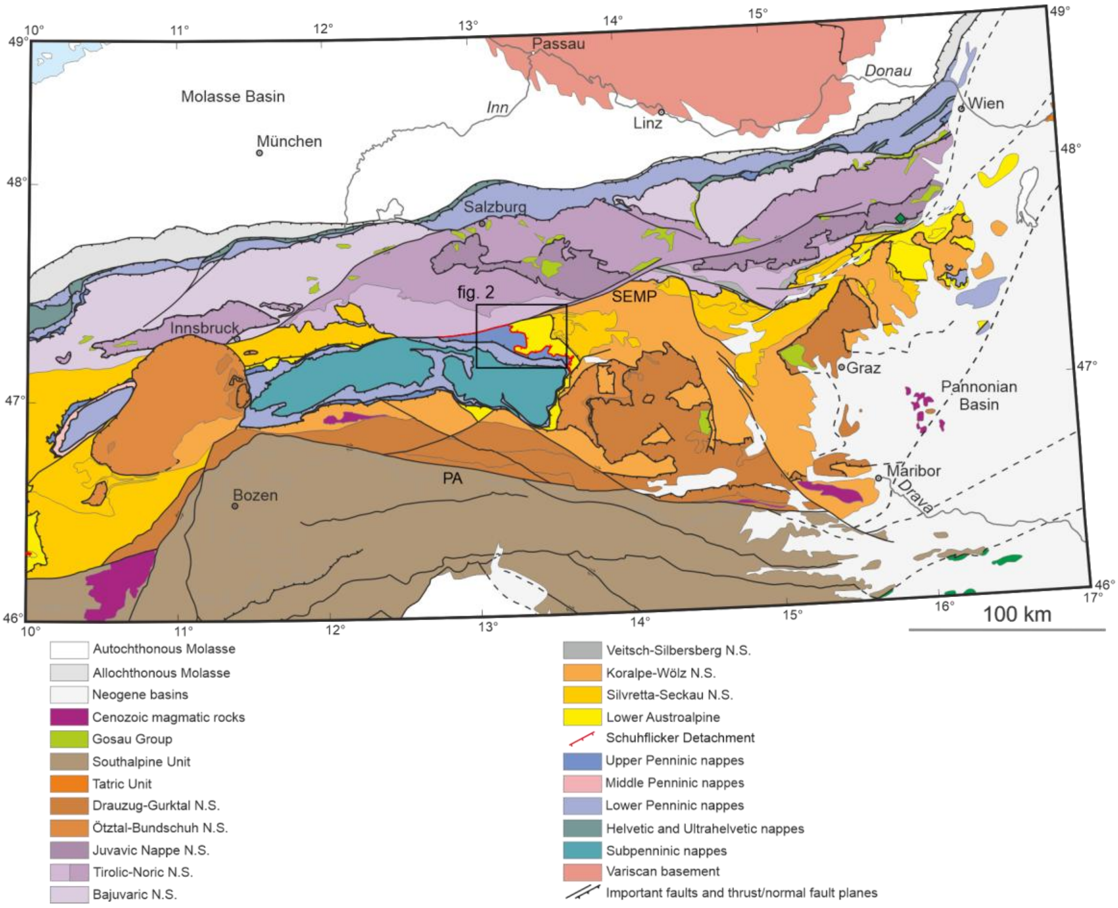

Figure 1: Tectonic map of the Eastern Alps. The black box shows the extent of the map in Figure 2. (modified after Schuster & Stüwe, 2022)

Jurassic-Cretaceous, intracontinental collision on the Adriatic microplate formed the Austroalpine Superunit consisting of the units of the Lower Austroalpine and the Upper Austroalpine. Ongoing collision led to the S- directed subduction of the Peninnic and the Sub-Peninnic units under the Adriatic continent, which led to high pressure metamorphism in those units (Frisch, 1979; Tricart, 1984).

The Tauern Window within the Eastern Alps represents one of the most prominent tectonic windows, exposing Sub Peninnic and Peninnic rocks within two metamorphic domes, the Western and Eastern Tauern Dome. The tectonic window is bordered by multiple large-scale faults towards the Austroalpine Superunit (Schmid et al., 2013). Laterally the Tauern Window is bound by two normal faults, respectively the west dipping Brenner normal fault on its western border and the east dipping Katschberg normal fault on its eastern border (Behrmann, 1988; Fügenschuh et al., 1997; Genser & Neubauer, 1989; Selverstone, 1988). On its northeastern margin the sinistral Salzachtal-Ennstal-Mariazell-Puchberg fault (SEMP) marks the border of the window, in the southeast the Tauern window is bordered by the Mölltal fault (Frisch et al., 2000; Frost et al., 2011; Kurz & Neubauer, 1996; Rosenberg & Schneider, 2008; Wang & Neubauer, 1998).

Within the Tauern Window, the units of the Penninic and the Subpenninic get divided into different nappe systems by their paleogeographic origin and their lithological characteristics. In the Subpenninic the nappe systems of the Venediger Duplex are derived from the European basement and sedimentary cover. The Modereck nappe system (see Figure 2) is part of the distal continental margin of the European continent and includes the Eclogite Zone of the Tauern

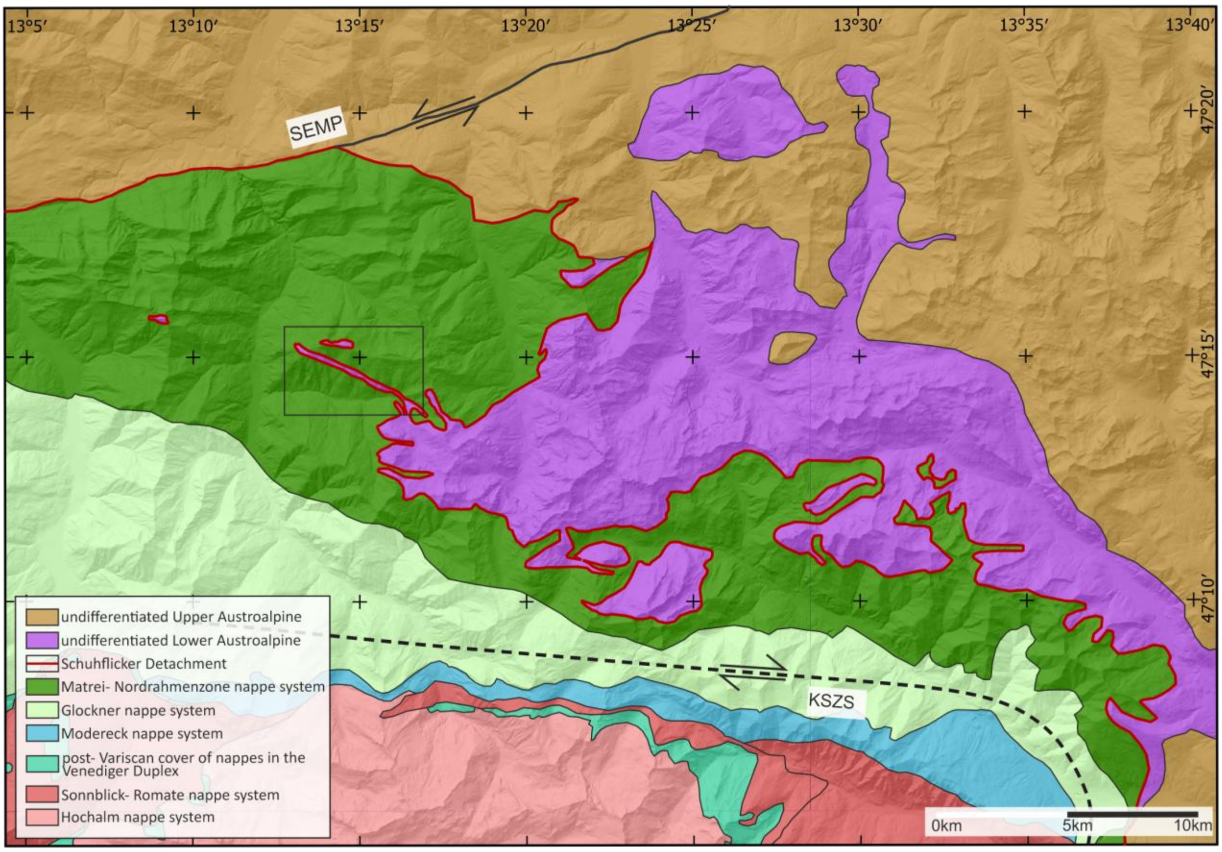

Figure 2: Tectonic map of the north-eastern Tauern window. The black box denotes the location of the map in Figure 3. KSZS: Katschberg Shear Zone System, SEMP: Salzachtal-Ennstal- Mariazell- Puchberg fault (modified after Schmid et al., 2013)

Window. The units attributed to the Penninic superunit are the Glockner nappe system and the overlying Matrei- Nordrahmenzone nappe system. Both units are comprised of similar ophiolite bearing lithologies with the difference, that the Matrei- Nordrahmenzone nappe system includes olistoliths that show similarities to the Lower Austroalpine. Palaeogeographically the Glockner nappe system represents units derived from an ocean branch that opened during the Early Cretaceous (Valais Ocean) and the Matrei- Nordrahmenzone units derived from a part of the Alpine Tethys that opened in the Middle Jurassic (Piemont Ligurian Ocean) (Schmid et al., 2013).

According to Schmid et al., 2013 the tectonic development of the Tauern window can be divided into 5 different deformation stages. In a first deformation stage (D1), which started in the Turonian (90Ma), the units of the Piemont-Ligurian ocean (i.e. Matrei- Nordrahmenzone nappe system) where accreted to the Austroalpine nappe stack. In a subsequent deformation phase D2, the units of the Valais Ocean as well as units from the most distal part of the European margin (i.e. Glockner nappe and parts of the Modereck nappe system) have been subducted and underwent eclogite facies overprint within an age range of 45-35 Ma (Glodny et al., 2005; Kurz et al., 2008; Schmid et al., 2013; Wiederkehr et al., 2008; Zimmermann et al., 1994) Deformation phase D3, according to Schmid et al., 2013 formed large scale isoclinal folds that lead to the decompression of the eclogitic units in a time interval from 38-32 Ma (Kurz et al., 2008). The D4 deformation is dominated by the formation of the Venediger Duplex and the subsequent "Barrow- type" metamorphic event called "Tauernkristallisation" which reached peak conditions of amphibolite facies and is dated at around 30Ma in the central Tauern Window (Schmid et al., 2013). The last defined stage of deformation (D5) includes processes related to indentation of the Dolomites indenter and the resulting doming and exhumation of the Tauern window by folding and along large-scale low angle normal faults (i.e. Katschberg and Brenner normal fault) (Schmid et al., 2013). It is important to note that the deformation phases D1-D5 of Schmid et al., 2013, do not represent the same phases of deformation as defined in chapter 4.2. These deformation phases are distinguishable deformation phases in the Nordrahmenzone, all belonging to the deformation phase D5 defined by Schmid et al., 2013.

3 Methods

3.1 Fieldwork and samples

Geological fieldwork focused on the structural geological and tectonic aspects of the units of the Nordrahmenzone. Furthermore, it focused on locating and mapping the border between the units of the Nordrahmenzone and the Lower Austroalpine. The fieldwork has been conducted on multiple N-S profiles parallel to the Großarl valley around the mountains *Saukarkopf* and *Schuhflicker* (see Figure 9)

Oriented samples from all identified units have been taken during fieldwork and have been prepared into thin sections for further microscopical investigations by the thin section laboratory of the Department of Geology at the University of Vienna.

3.2 Microstructural analysis

From the samples taken thin- sections in two different orientations have been made and analysed for their microstructural contents on a *Nikon Optiphoto2- Pol* optical microscope. Scans of the thin sections have been made with a *Nikon Super-Coolscan 5000ED* slide scanner. For single pictures and photomosaics of important microstructures a *Leica DM4500P* microscope with *a Leica K5C* camera and an automatic XY stage was used.

3.3 Raman micro- spectroscopy of carbonaceous materials

For peak temperature estimation, Raman micro- spectroscopy of carbonaceous materials was done on three graphitic schists and meta-conglomerates. In preparation for the measurements, the graphite was separated from the rock matrix by mechanical crushing and the hydrochloric and hydrofluoric acid treatment described in Rantitsch et al.(2004). Raman spectroscopy was done on a *LabRam HR Evolution Raman* spectrometer with a 532nm Laser and a diffraction grating of 1800 grooves/mm. Raman spectra were taken in a Range of 700-2000 cm^{-1} and an acquisition time of 20s with two acquisitions per measuring point. For each of the samples a minimum of 20 points has been recorded. The data was analysed by Professor Dr. Gerd Rantitsch from the University of Leoben using the methods described in Rantitsch, 2023 and Lünsdorf et al., 2017.

3.4 Optical cathodoluminescence

For the acquisition of optical cathodoluminescence (CL) images a hot cathode CL microscope of the type *lumic HC5-LM* with a *CCD Kappa PS 4 / 40* camera at the Department of Lithospheric research at the University of Vienna has been used. For the imaging, four polished thin sections of calcitic mylonites have been coated with 4nm of carbon. The images have been taken with an acceleration voltage of 14keV, a probe current of 0,2 mA and exposure times between 181ms and 1.10s. For the stitching of the photomosaics and shading correction the software FIJI in the version 1.54 has been used.

4 Results

4.1 Mapping

For this work a new geological map of the area around Mt. Saukarkopf has been made (Figure 3). The map has been compiled by using the data taken on two of the profiles during the fieldwork as well as using the old map of Peer & Zimmer, 1980. For the compilation of the map, three distinguishable lithologies of the Lower Austroalpine and five of the Nordrahmenzone have been identified. In the Nordrahmenzone the Black phyllites and the Marble mylonite (Klammkalke) have been mapped as one unit as there are changes between these lithologies, that cannot be resolved at the scale of the presented map. The map shows the syncline containing the dolomites of Mt. Saukarkopf (northernmost Dolomite Klippe) as well as a few other synclines containing the different units of the Lower Austroalpine on the southern flank of Mt. Saukarkopf. In the version of the map presented below, only foliations and stretching lineations of the mylonitic deformation (D_1) are presented. A further version of the map containing RSCM data is presented in chapter 4.4 (Figure 23). The map and all coordinates in this work are given in the WGS 1984 UTM 33N coordinate system.

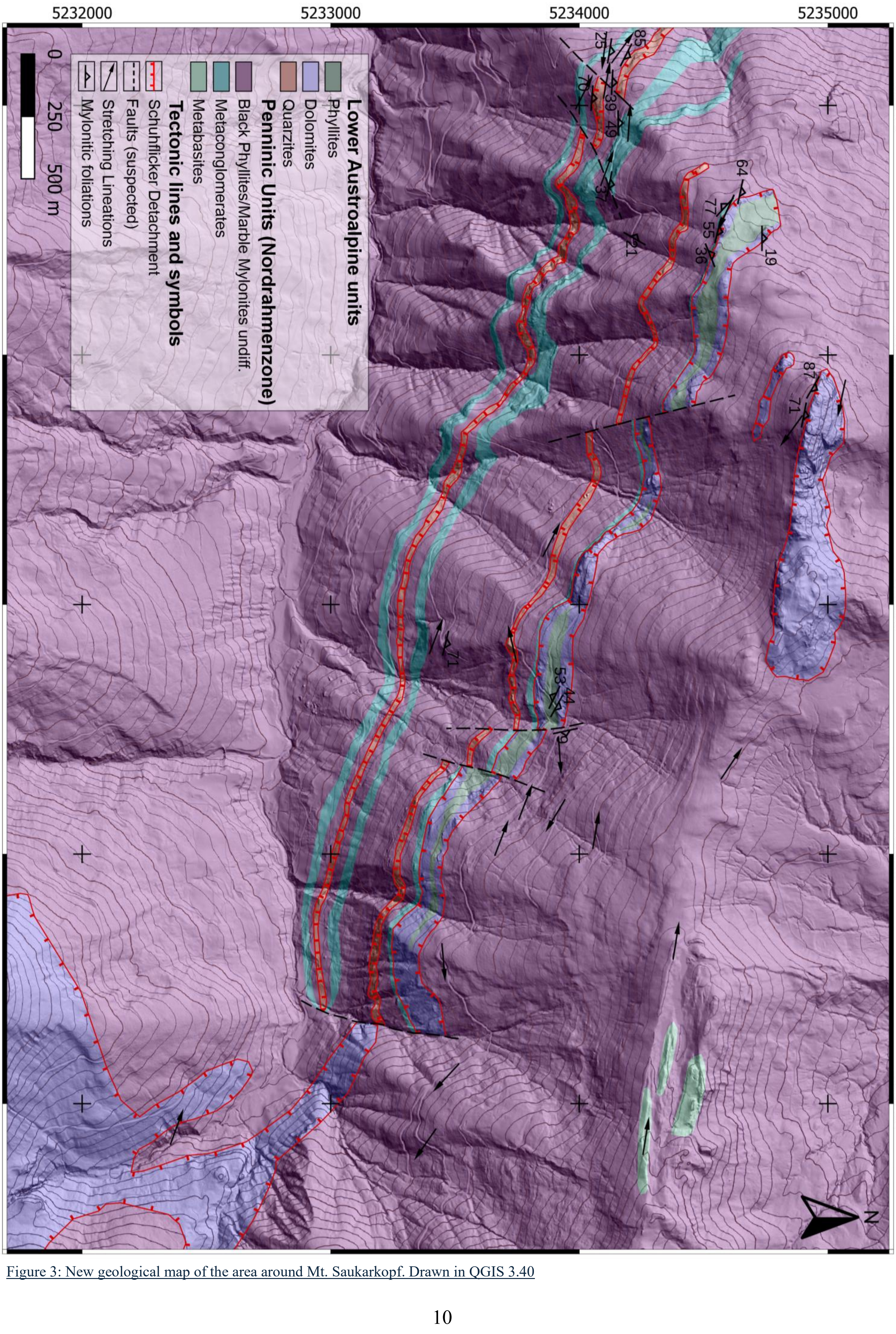

Figure 3: New geological map of the area around Mt. Saukarkopf. Drawn in QGIS 3.40

4.2 Structural observations in the field

For this study we define four deformation stages that can be distinguished based on field observations as well as cross cutting relationships of planar and linear structures.

4.2.1 D_1- mylonitization

The deformation phase D_1 is represented by mylonitic fabrics that can be found in all the different lithologies of the Peninnic units found in our research area. The mylonites all show a mylonitic foliation (s1) with a stretching lineation (l1). The dip of s1 foliations varies quite a lot throughout the area around Mt. Saukarkopf, ranging from generally steeply dipping mylonitic foliations, to locally subhorizontal foliations (see Figure 4a). As seen in Figure 4a dip directions vary also quite a lot throughout the area, but generally the poles scatter around N-S striking great circle with a maximum of foliations dipping towards N. The measurements of stretching lineations show a well-defined maximum subhorizontal in a NW-SE direction as shown in Figure 4b.

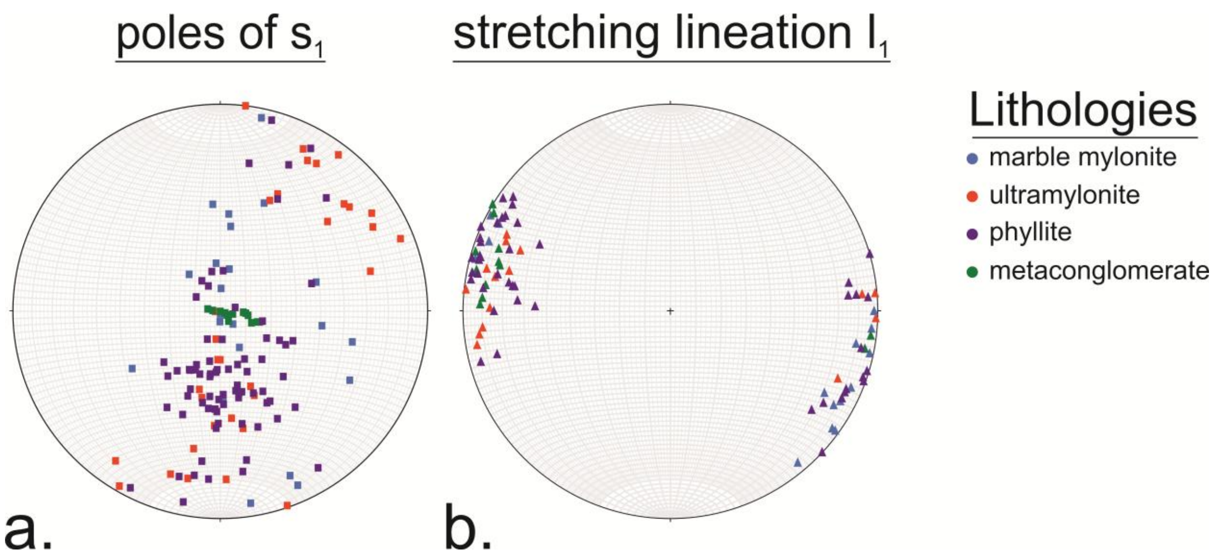

Figure 4: Lower hemisphere, equal area stereographic projections of the poles to the foliation s1 (a.) and stretching lineations l1 (b.) colour coded after the main lithologies found in the area.

Structurally it can be observed in the field that the intensity of the mylonitic foliation differs throughout the research area and within the different lithologies (see Figure 5a-d). In structurally lower levels, the mylonites have a lot of left over components (see Figure 5a) and layers that show pinch and swell geometries of stretched quartz and calcite veins (see Figure 5b) that can often be used as shear sense indicators (Figure 6). Towards higher structural levels the mylonitic fabric gets more intense and no clasts are preserved in the fine ultramylonitic layering (see Figure 5c&d).

Figure 5: Examples for the appearance of the mylonitic foliation in different lithologies **(a)** Calcite metaconglomerate showing mylonitic foliation and components deformed into pinch and swells (UTM33N: 358883/5235254).**(b)** Marble mylonite with a subvertical mylonitic foliation (S_1) and an E-W striking stretching lineation (L_1) White layers have been stretched and deformed into pinch and swells. (UTM33N: 358811/5235300). **(c&d)** Marble ultramylonites with a steep N-dipping mylonitic foliation. (UTM33N: 367506/ 5233945)

As mentioned above, shear sense indicators of the mylonitic deformation D1 can be found in all the different lithologies. Within the marble mylonites they mainly consist of pinch and swell objects in calcite layers or rotated clasts, that show monoclinic symmetries or have been rotated. Examples for these shear sense indicators are given in Figure 6a-f with a few examples of sigmoids as well as a winged inclusion (marked with *a* in Figure 6b). In other lithologies mainly in the different phyllonites found in the Penninic, shear senses are mostly recorded by c' type shearbands and scc' fabrics (see Figure 7a-f). A shearband was also found in an outcrop of Penninic metabasites (Figure 7a&b) showing a top to E shear sense. Throughout the area, shear sense indicators showing seemingly contradicting shear senses have been found. In mylonites with shallower dips, all the shear senses recorded show a top to the E ductile shear sense (see Figure 6c-f and Figure 7a-b). In outcrops where mylonites are dipping subvertical dextral shear senses (Figure 6a-b and Figure 7c-d) as well as sinistral ductile shear senses (Figure 7e-f) have been recorded.

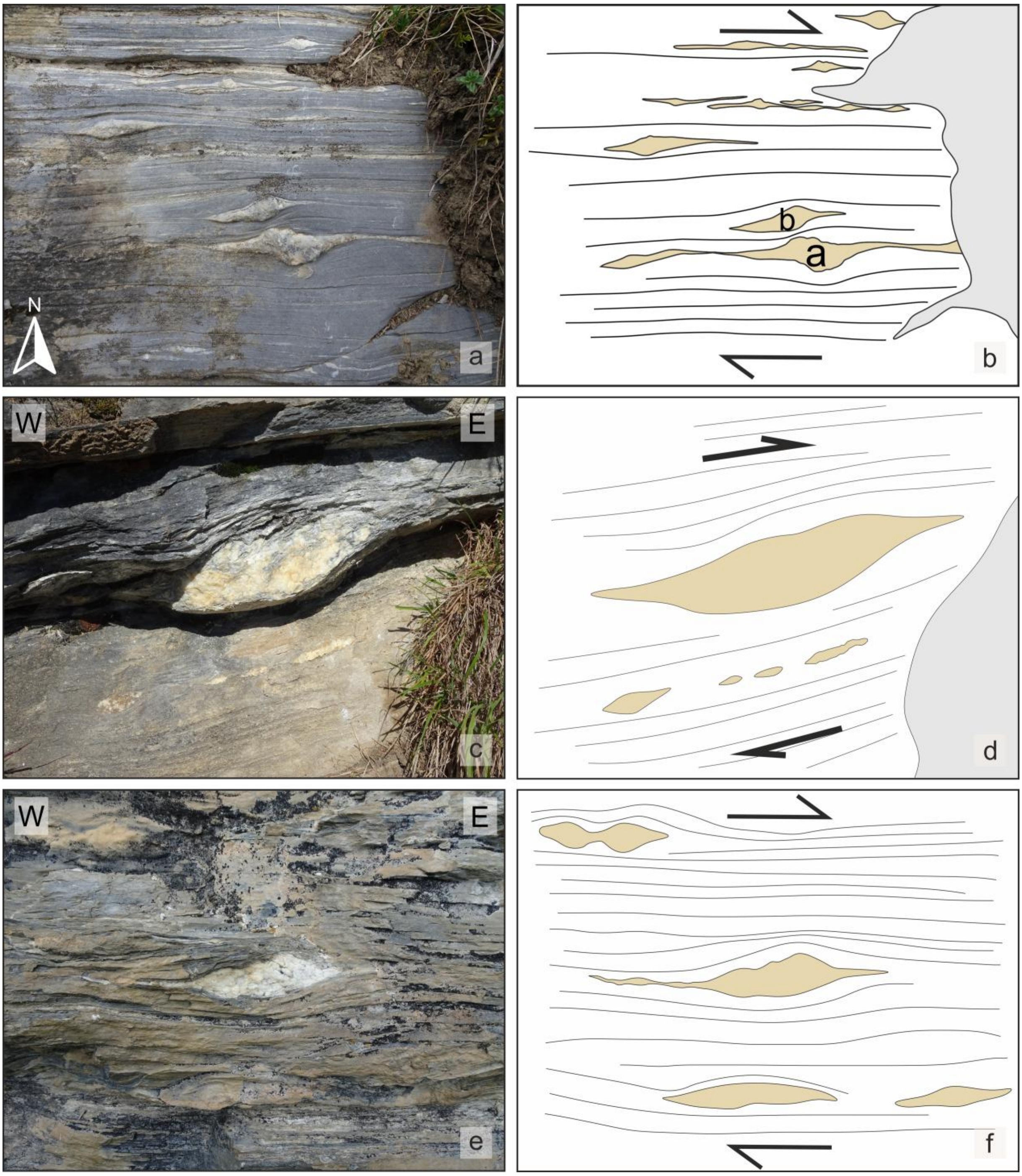

Figure 6: **(a&b)** Picture and interpretative sketch of different shear sense indicators in boudinaged calcite layers in a marble mylonite of the Nordrahmenzone. The winged inclusion (a) and the sigmoid (b) both record an apparent dextral shear sense. (UTM33N: 365147/5233984) **(c&d)** Picture and interpretative sketch of a calcite sigmoid showing top to E ductile shear sense in a marble mylonite. (UTM33N: 358804/523530) **(e&f)** Calcite pinch and swells in a marble mylonite, one deformed into a sigmoid showing top to E shear sense. (UTM33N: 365234/5233930)

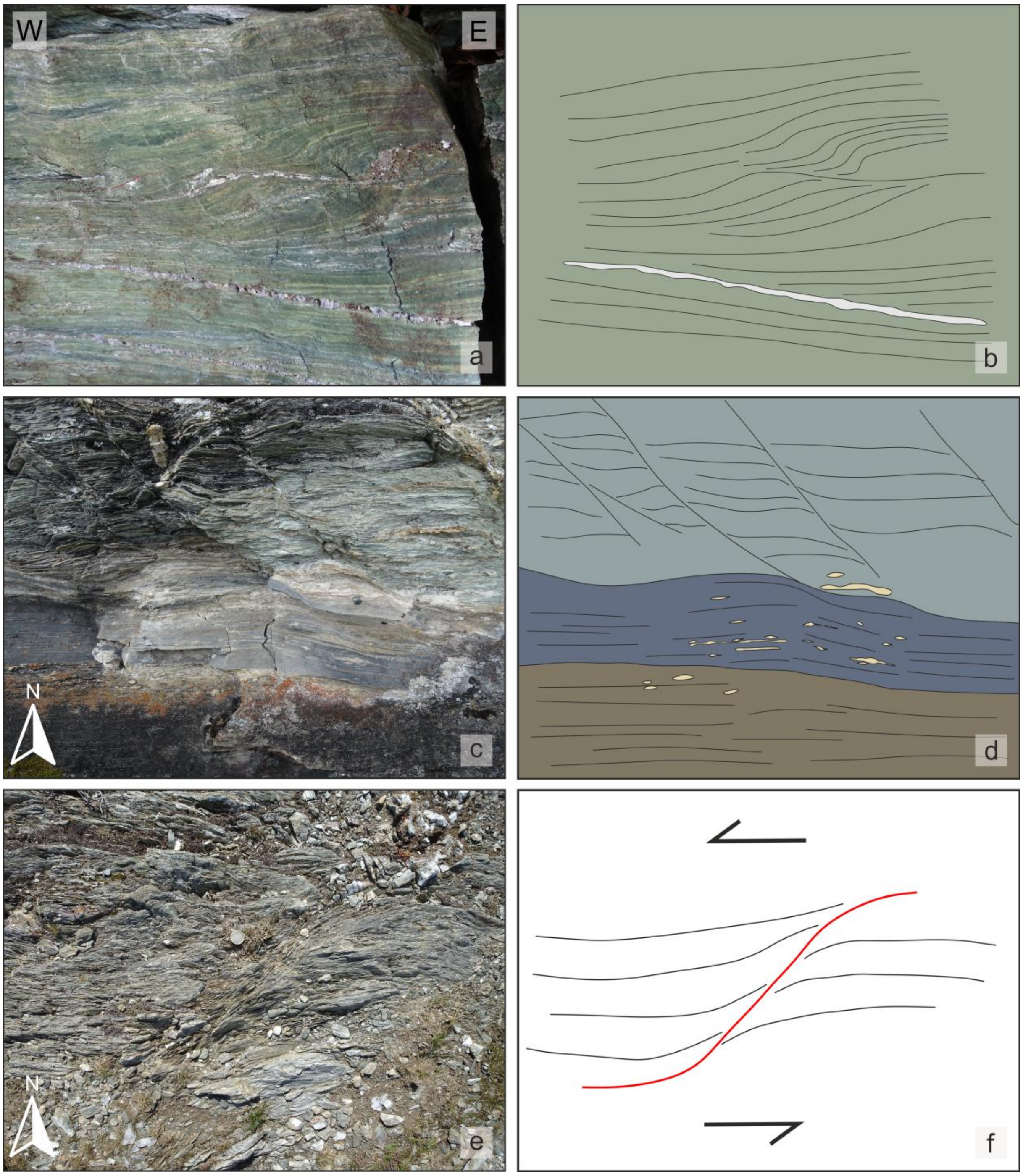

Figure 7: **(a&b)** C' type shearband in metabasites showing top to E shear sense (UTM33N: 369133/5234266) **(c&d)** scc' fabric in Peninnic phyllonites (grey colour in sketch) structurally above marble mylonites (blue) with boudinaged calcite layers, that show some sigmoid shapes and metaconglomerates (brown). All shear sense indicators show a dextral ductile shear sense. (UTM33N: 365409/5234521) **(e&f)** Shearband in Peninnic phyllites showing sinistral shear sense (UTM33N: 368987/5234265)

At the highest structural levels of the Penninic units of the research area, the structures associated with mylonitization intensify. The highest intensity of deformation can be observed directly below the border between the Peninnic units and the Lower Austroalpine units. At Mt. Schuhflicker a zone of highly deformed marble mylonites can be found, bordered by Lower Austroalpine Dolomites, that have not been deformed ductile during D1 (see Figure 8a-b). Within this zone, high strain ductile structures associated with the mylonitic deformation D1 can be found like isoclinal folds or sheath folds (see Figure 8e-f). Furthermore, it can be observed that the dolomite above the ultramylonites has been deformed by brittle deformation that can be observed in cataclasites, that sometimes also show a foliation (Figure 8c-d). Similar ultramylonites that are bordered by brittle deformed dolomite can also be found below the summit of Mt. Saukarkopf (Figure 5c-d) as well as in other parts of the research area.

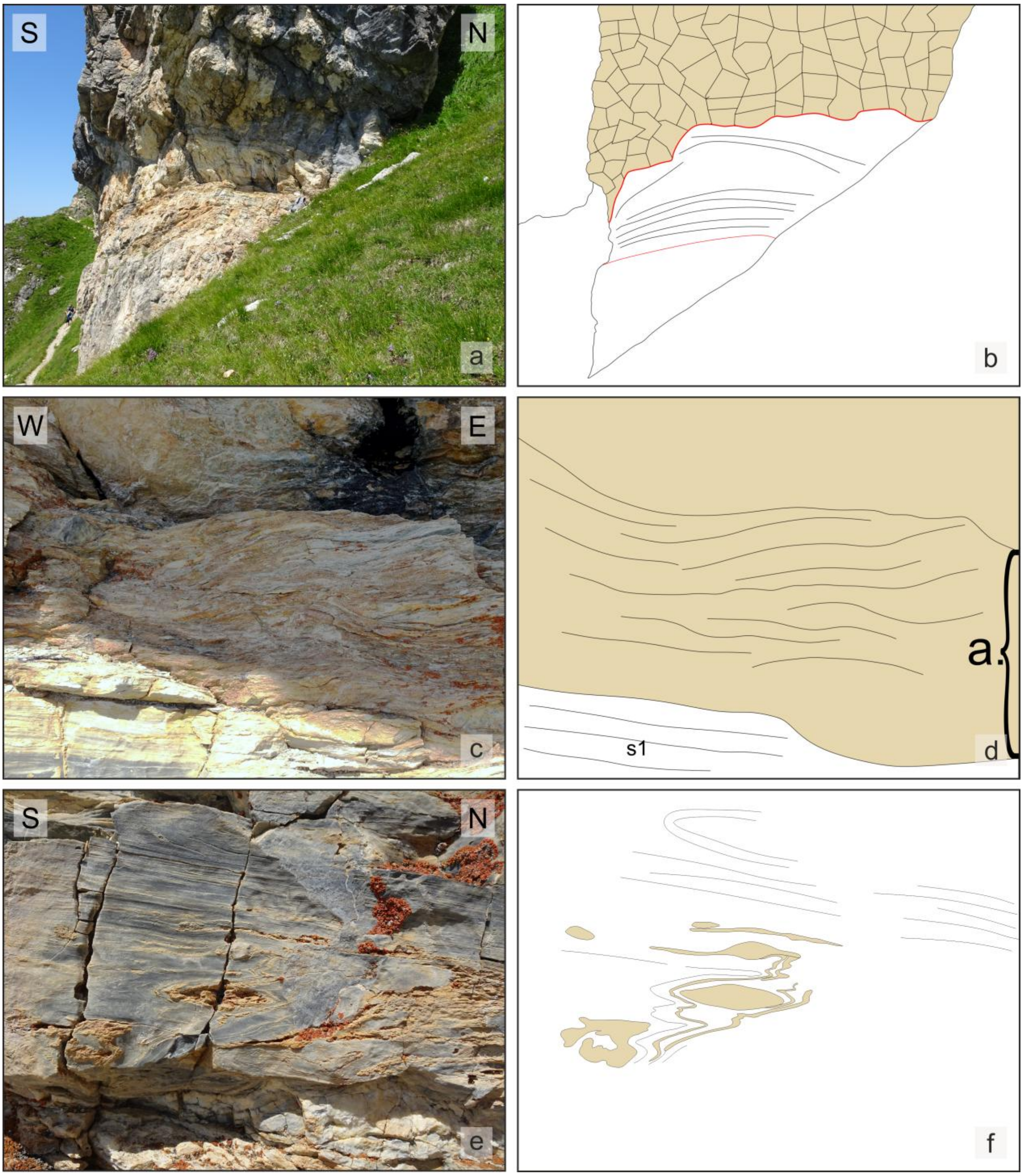

Figure 8: **(a&b)** Contact between Lower Austroalpine in the hanging wall and Peninnic units in the footwall. The detachment zone (between the 2 red lines) is made up of marble ultramylonites and foliated cataclasites. (UTM33N: 360246/5235867). **(c&d)** Foliated cataclasites in Lower Austroalpine dolomite (a.) in the detachment zone above marble ultramylonites. (UTM33N: 360246/5235867) **(e&f)** Sheath fold (a.) within folded detachment ultramylonites. Layers of dolomitic composition within the sheath fold and in the marble mylonites deform brittle (brown colour in sketch). (UTM33N: 360246/5235867)

4.2.2 D_2- N-S shortening

A second phase of deformation is characterized by folds with a NW-SE trending fold axis and an axial plane, that dips steep towards north as can be seen in the stereographic projection in Figure 9c. These folds make up the regional scale folding within the research area, folding also the boundary between the Penninic and Lower Austroalpine units. The dolomites of Mt. Saukarkopf and Mt. Schuhflicker lie inside of regional scale synforms as shown in Figure 9a&b.

At the outcrop scale higher order folds of these regional scale f2 folds, get refolded by a later generation of folds described in 4.2.3. (see Figure 10a-b).

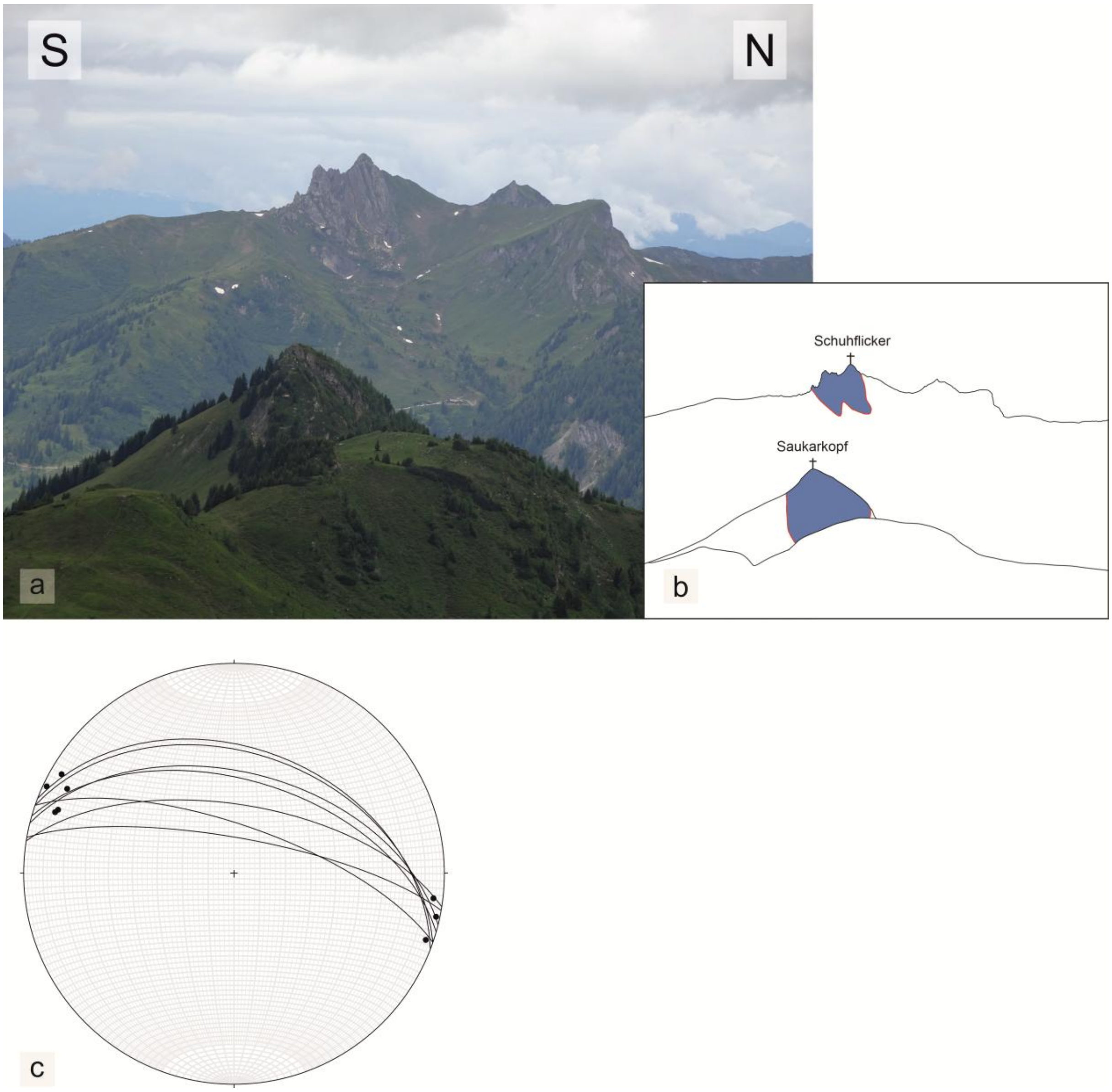

Figure 9: **(a&b)** Overview picture from the Gründegg looking west showing the tectonic klippen of the Saukarkopf and the Schuhflicker. Both klippen consist of Lower Austroalpine Dolomites (mapped as "Wettersteindolomit") that is lying inside large scale f2 synforms of Penninic rocks. The border between the two units is made up of marble ultramylonites and dolomite cataclasites (see Fig. 8). (UTM33N: 369985/5234331) **(c)** Lower hemisphere, equal area stereographic projection showing steep north dipping axial planes of f2 folds and NW-SE trending fold axes.

The folds are also associated with a pervasive axial plane cleavage (saxpl2) shown in Figure 10b.

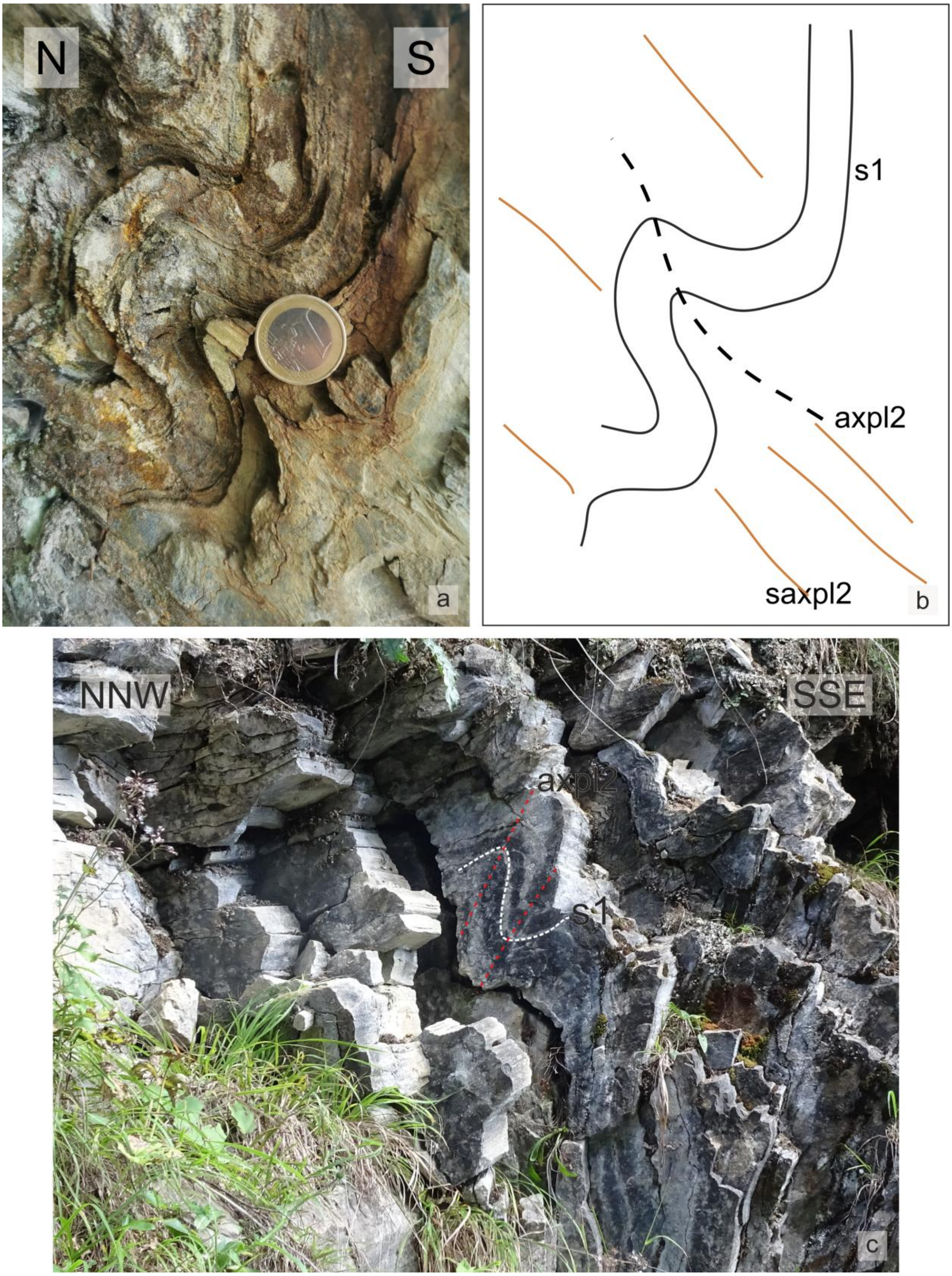

Figure 10: **(a&b)** F2-type folds folding the mylonitic foliation (s1). The folds have been slightly refolded by f3-folds with subhorizontal axial planes. The folds are associated with a pervasive axial plane cleavage(saxpl2). (UTM33N: 364791/5234177) **(c)** Folded marble mylonites with south vergent f2 folds folding the mylonitic foliation s1 (UTM33N: 358809/5235303)

4.2.3 D_3- vertical flattening

A third phase of deformation that can be distinguished in the area is characterized by another generation of folds (f3). These folds show subhorizontal or N and S shallow dipping axial planes and fold axes that trend NW-SE, parallel to the stretching lineations of D_1 and the fold axes of f2 folds. The folds tend to show a wide opening angle as can be recognized in Figure 11a&c. They are also often associated with a pervasive axial plane cleavage that is particularly strong in the phyllites of the Nordrahmenzone and there often makes up the main recognizable foliation (see Figure 11b).

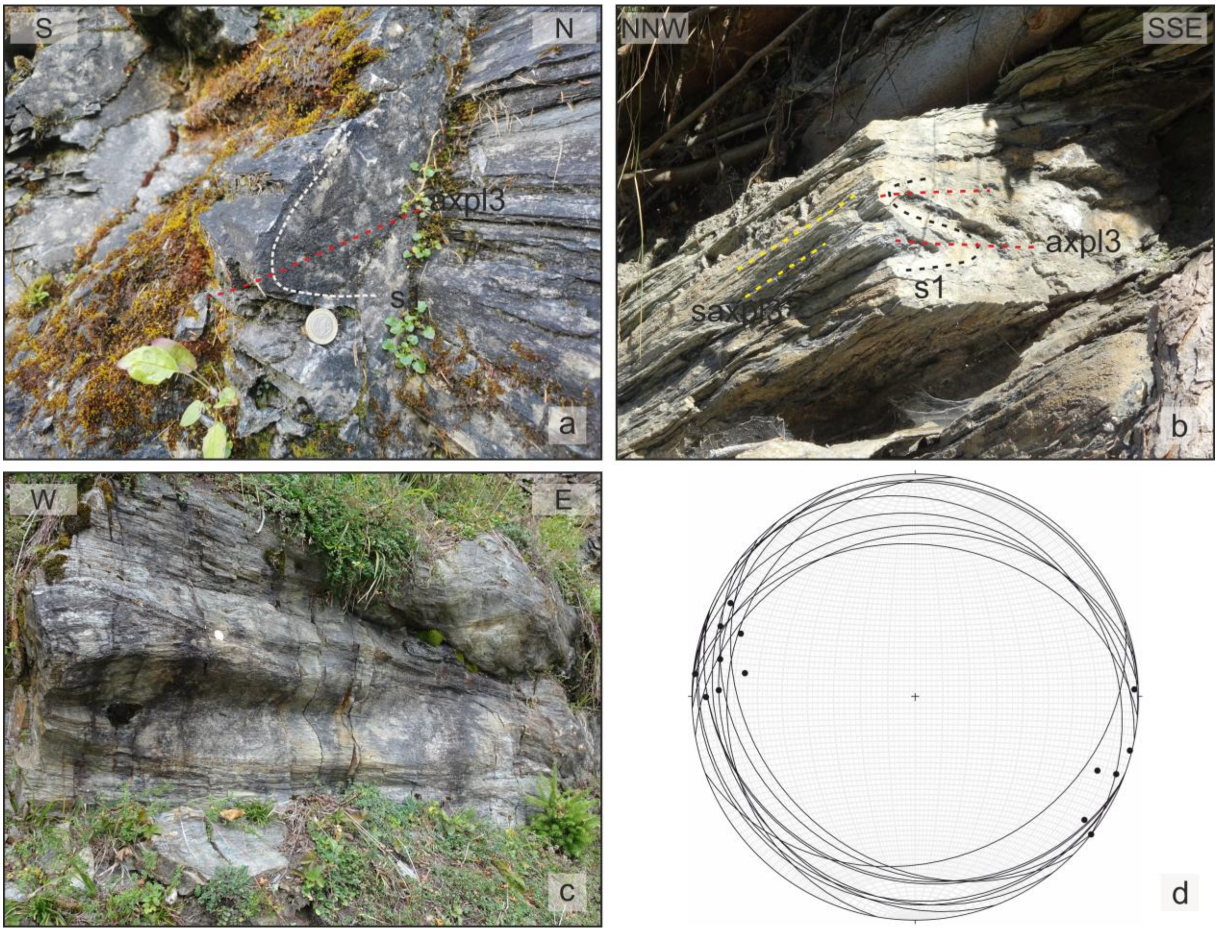

Figure 11: **(a)** Folded marble mylonite showing a f3 fold with a subhorizontal axial plane, NW-SE trending fold axis and a wide opening angle. (UTM33N: 365809/ 5236370) **(b)** f3 fold in phyllites folding the mylonitic foliation s1. A pervasive axial plane cleavage (saxpl3) of the f3 folds becomes the main recognizable foliation in that outcrop especially in the hinge areas of the fold. (UTM33N: 357560/5235601) **(c)** 3D view of a f3 fold in marble mylonites. The 3D representation of the open folds can be seen by looking onto the folded foliation plane s1. (UTM33N: 358622/5235433) **(d)** Lower hemisphere, equal area stereographic projection of the NW-SE trending fold axes (points) and the subhorizontal axial planes (great circles) of f3 folds.

4.2.4 D_4- late stage top-E extension

A fourth stage of deformation that can be distinguished in the area is defined by its cross-cutting relationships with the structures formed in the deformation phases D_1-D_3. Structures that are associated with that phase of deformation record an ongoing late stage of E-W extensional deformation. The most common structures that can be found in the area, that are formed by D_4 are C' type shearbands, that crosscut all earlier structures D_1-D_3 (see Figure 13a-d). Those late shearbands always show a dip of 10-40° towards east and record a top to E deformation (see Figure 12). Other structures that show a later stage of E-W extension are subvertical, N-S striking extension veins that mostly consist of calcite as can be seen in Figure 13a-b. In some outcrops of the area, conjugated brittle-ductile normal faults can be found (see Figure 13e-f)

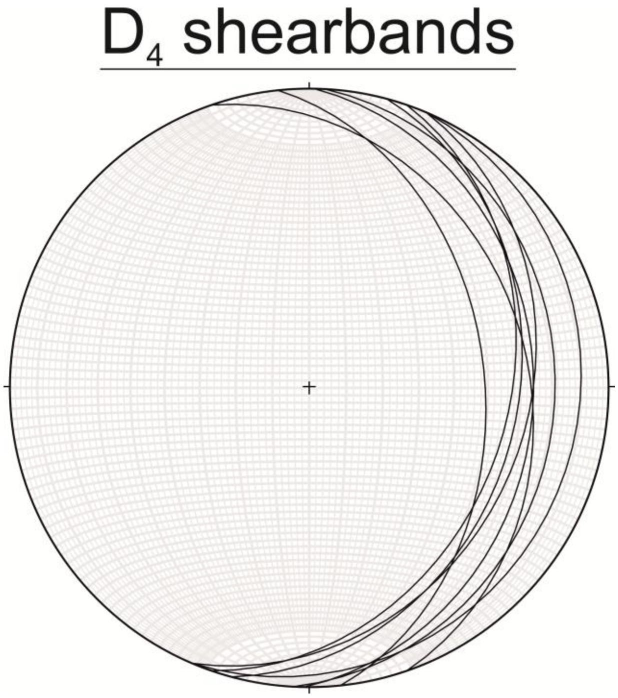

Figure 12: Lower hemisphere, equal area stereographic projection of planes of D4- shearbands.

where the foliation of the mylonites is bend into the fault, acting as an indicator of the movement direction.

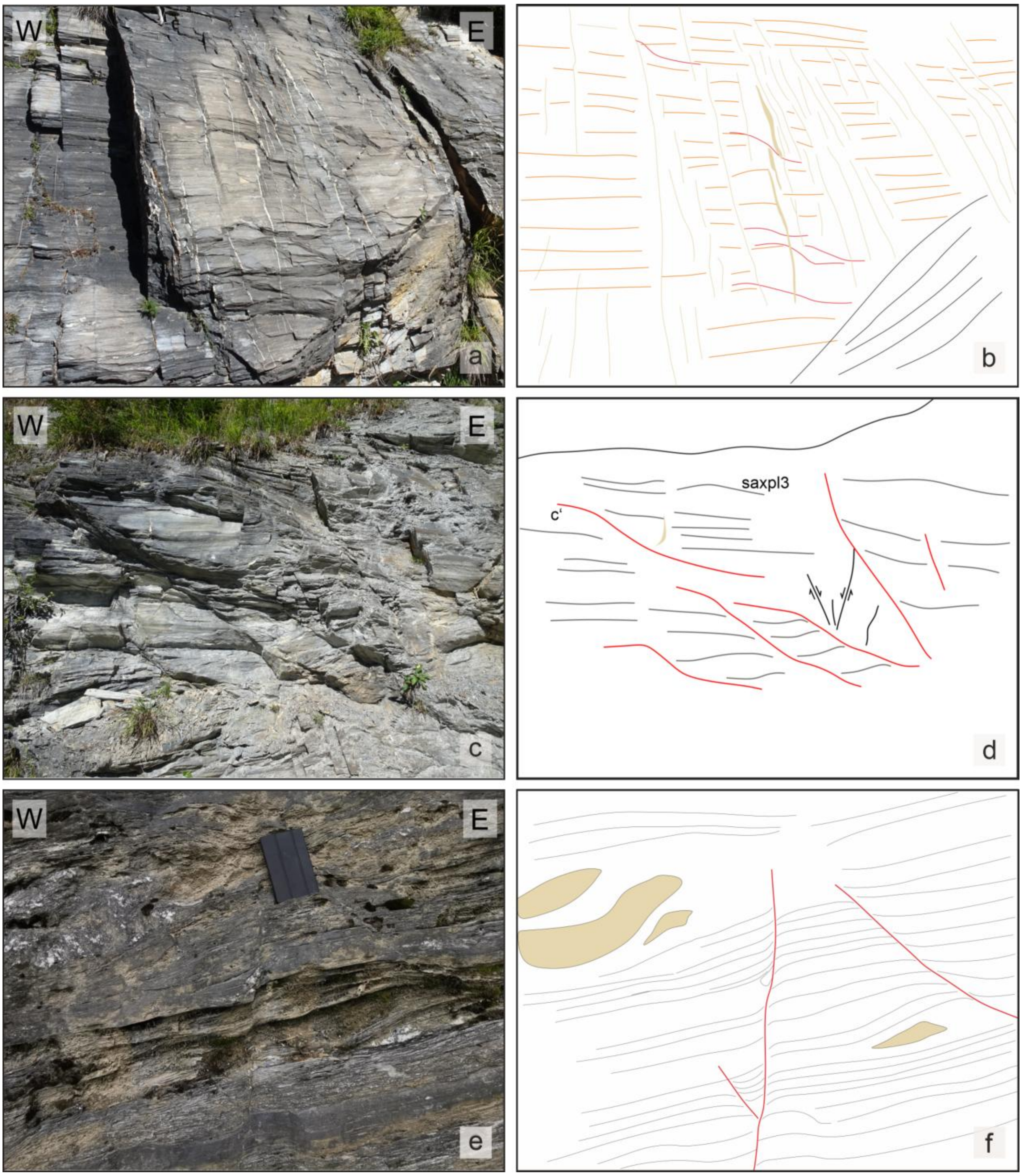

Figure 13 **(a&b)** Subvertical N-S striking calcite veins and c'type shear bands cutting through F3 axial plane cleavage (orange foliation in sketch), recording late E-W extension. (UTM33N: 357467/5236539) **(c&d)** C'type shearbands in folded marble mylonites. The subhorizontal foliation represents an axial plane cleavage (saxpl3) of F3-type folds. The shearbands cut the axial plane cleavage as well as the folds, showing ongoing top to E shearing after folding. (UTM33N: 358699/5235367) **(e&f)** Conjugated brittle-ductile normal faults. The mylonitic foliation s1 bends into the movement direction of the normal faults acting as a shear sense indicator. (UTM33N: 365319/5234122)

4.3 Microstructural observations

Thin sections prepared from samples collected in the field reveal microstructures corresponding to all macroscopically described deformation phases described in Chapter 4.2. The specific microstructural characteristics vary depending on the lithology and the location from which the samples were taken. Microstructures associated with the D_1 deformation phase are present in all samples from Peninnic units. Two metaconglomerate samples were collected from lower structural levels, and their microstructures are shown in Figure 14 through photomicrographs and photomosaics. Sample TW12_23 is a metaconglomerate with a matrix composed almost entirely of calcite, containing porphyroclasts of calcite (Figure 14c), quartz (Figure 14e), and dolomite (Figure 19b). In contrast, sample TW04_23 exhibits a more heterogeneous matrix, primarily composed of quartz and calcite, along with packages of white mica. Its components are like those in TW12_23, mainly quarzitic, calcitic, and dolomitic, with additional fragments of radiolarite (Figure 14b).

In TW12_23, the calcite matrix is fully dynamically recrystallized into layers with varying grain sizes (Figures 14c and 14e). The recrystallized calcite grains are elongated and display an oblique shape-preferred orientation (SPO), indicating top-to-the-east ductile shearing. In TW04_23, recrystallization is observed only in the quartz-rich portions of the matrix, while the calcite grains remain relatively large (up to 1 mm) and exhibit idiomorphic to hypidiomorphic grain boundaries (Figure 14a). The components of both metaconglomerates show diverse geometries: some are stretched and display pinch-and-swell structures (Figure 14c), while others exhibit sigmoidal shapes consistent with top-to-the-east ductile shearing (Figure 14d).

Three samples of pure marble mylonites were collected and prepared as thin sections. To investigate their microstructures, optical CL photomosaics (see Chapter 3.4) were acquired in addition to XPL and PPL images. Two of these samples (TW04_24 and TW05_24) were taken from the immediate vicinity of the boundary between the Penninic and Lower Austroalpine units. Both exhibit a fine-grained, ultramylonitic calcite fabric.

Sample TW05_24 displays the highest degree of mylonitic deformation, characterized by fully recrystallized calcite grains arranged in layers of varying fine grain sizes. At the edge of the thin section, the sample was ground extra thin, allowing clear visualization of grain boundaries and calcite grain shapes. As shown in Figures 15a and 15b, the recrystallized grains are predominantly highly elongated, with further recrystallization producing nearly isometric

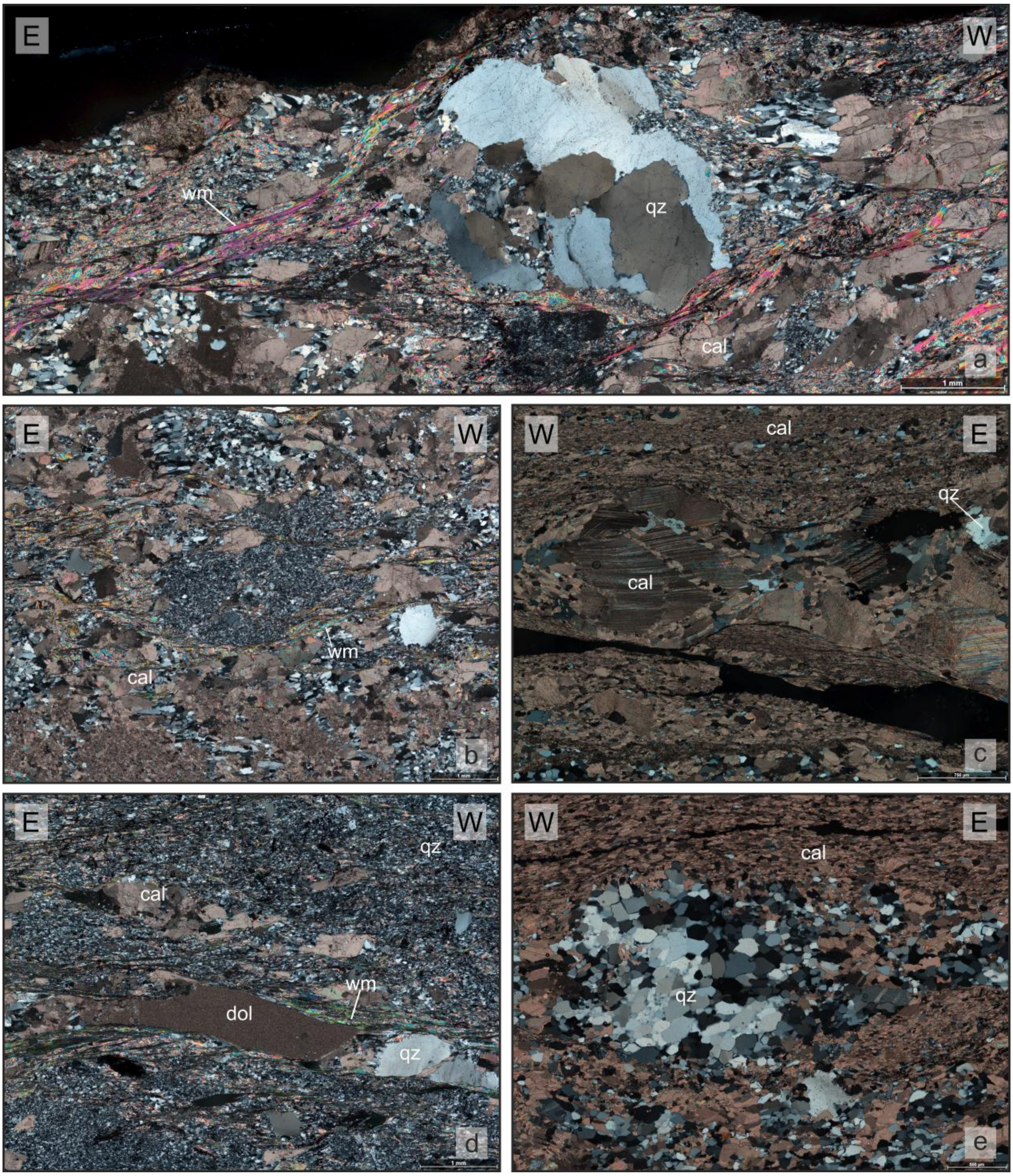

Figure 14 Cross-polarized light (XPL) photomicrographs of metaconglomerates from the Penninic unit. **(a)** Recrystallizing quartz clast in sample TW04_23, hosted in a matrix dominated by quartz and calcite. White mica accumulates in layers along the clast–matrix boundary. (UTM33N: 367308/5233844) **(b)**Possible radiolarite clast in sample TW04_23 **(c)** Stretched calcite clast in sample TW12_23 exhibiting pinch-and-swell structures. A vein filled with calcite and quartz transects the clast. The matrix is composed mainly of calcite, recrystallized into layers with variable grain sizes (UTM33N: 367308/5233844) **(d)** Dolomite, calcite, and quartz clasts in sample TW04_23, embedded in a fine-grained recrystallized quartz matrix. Clasts labelled "dol" and "cal" display sigmoidal geometries indicative of top to the east ductile shearing. **(e)** Partially recrystallized quartzite clast in a calcite-rich metaconglomerate. The recrystallized calcite matrix exhibits a shape-preferred orientation (SPO), consistent with top to the east ductile deformation. (UTM33N: 367308/5233844)

grains as small as ~1 μm. The largest grains in Figure 15a reach approximately 0.5 mm in length and exhibit pronounced elongation. These recrystallized grains show an SPO nearly parallel to the main foliation and are largely devoid of deformation twins. Additionally, TW05_24 contains

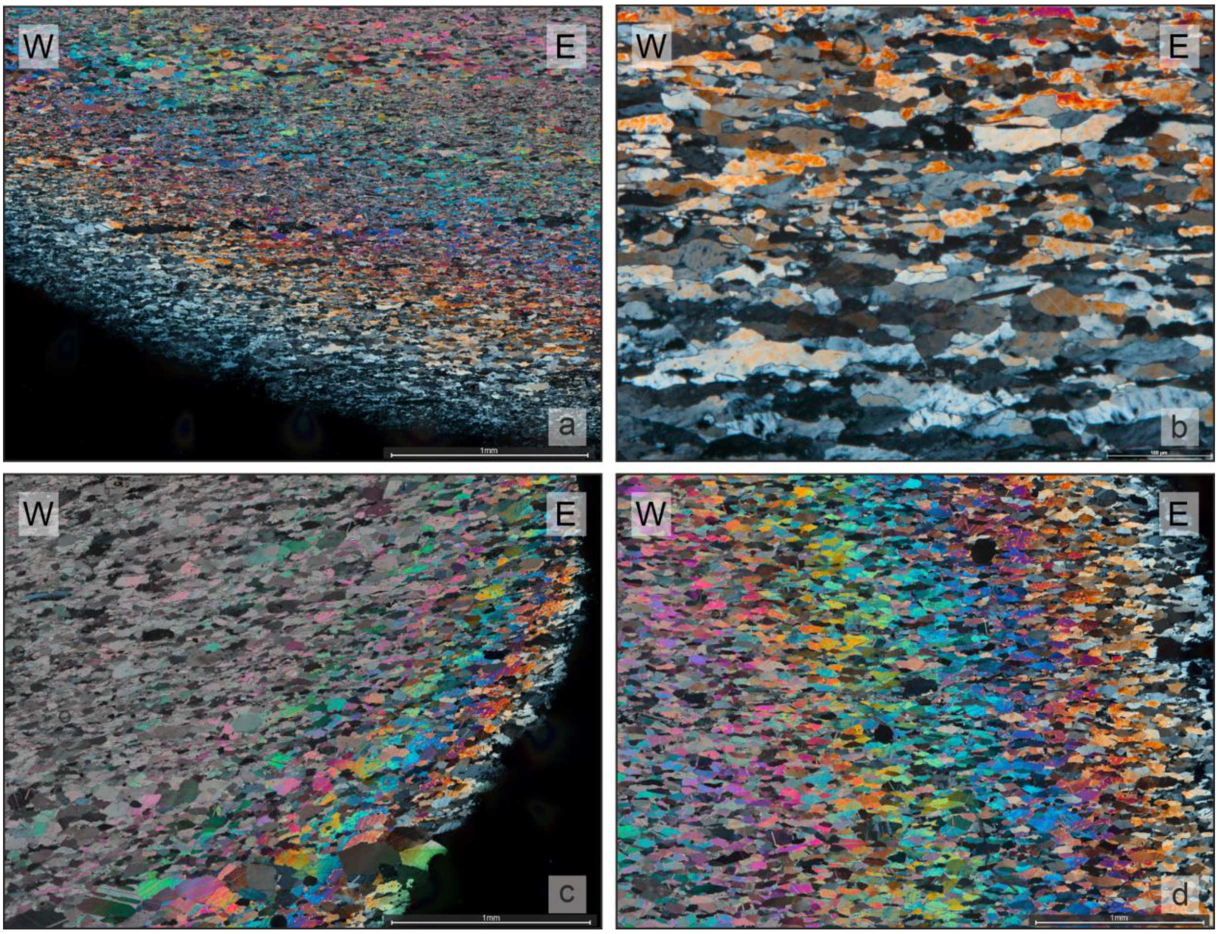

Figure 15: Photomosaics and photomicrographs of different marble mylonite samples. **(a)**XPL photomosaic of the thinning corner of the thin section of sample TW05_24 to show grain boundaries and grain shape of calcite **(b)** detail XPL photomicrograph of TW05_24 taken with 20x lens showing elongate recrystallized grains varying in grain size >100µm to down to ~1µm **(c)** XPL photomosaic of sample TW04_24 **(d)** XPL photomosaic of sample TW04_23

a layer of calcite with significantly larger grain sizes, which is stretched and displays a pinch-and-swell geometry. Within this layer, calcite crystals up to 1 mm in size with abundant twinning are observed. A CL photomosaic of this layer, shown in Figure 16 alongside a PPL photomosaic of the same area, reveals that CL intensity is markedly higher in the pinch-and-swell layer compared to the surrounding recrystallized matrix. The main mylonitic fabric exhibits a homogeneous, low CL signal, whereas the stretched layer shows generally higher intensity, with localized peaks in individual grains and along twin lamellae of large calcite crystals. Above this layer, another coarse-grained zone lacking signs of dynamic recrystallization is present. This zone shows lower CL intensity than the surrounding calcite, with slightly elevated intensity along grain boundaries.

Sample TW04_24 shares many features with TW05_24 but generally exhibits larger grain sizes, as illustrated in Figures 15a and 15c. The recrystallized grains are elongated and display an SPO oblique to the main foliation, indicating a top-to-the-east sense of ductile shear. Compared to TW05_24, more twins are present in the recrystallized grains. This sample also contains several coarse-grained layers with pinch-and-swell geometry. One such layer is depicted in Figure 17, where a sigmoid structure consistent with top-to-the-east shear is visible. It includes large calcite grains with abundant twins and a strain shadow composed of calcite grains approximately 0.1 mm in size.

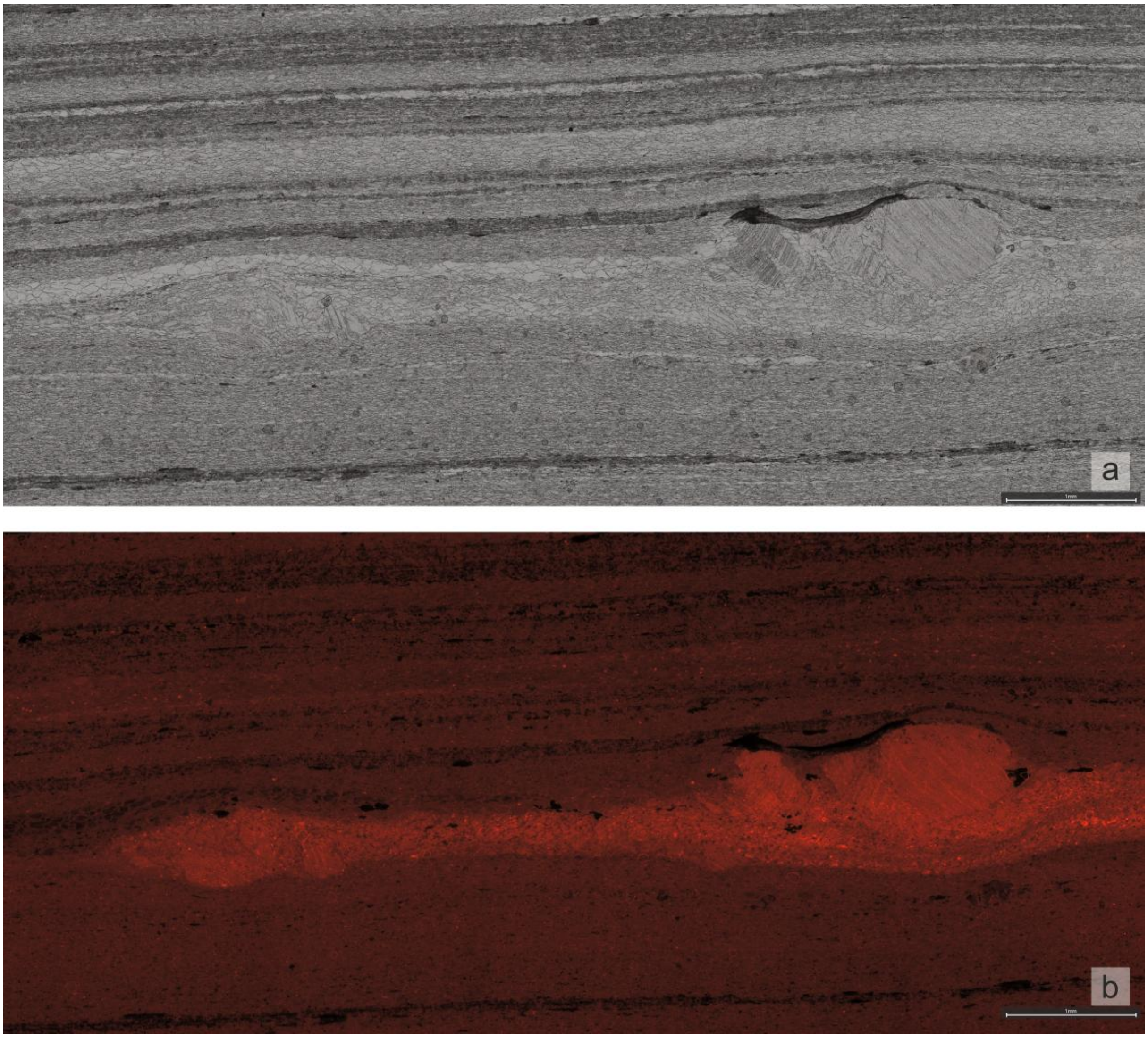

Figure 16: **(a)** PPL photomosaic of marble ultramylonite showing a layering of different grade of recrystallization **(b)** optical CL photomosaic of sample TW05_24 taken with an exposure time of 679ms. (UTM 33N: 366135/5234950)

An optical CL photomosaic of TW04_24 reveals generally higher CL intensity, attributed to the shorter exposure time used compared to TW05_24. As in the other ultramylonitic sample, the highest CL intensities are found in coarser-grained regions. Fully recrystallized layers show homogeneous CL signals, while areas with larger grains exhibit more heterogeneous intensity. The highest CL values occur in the large crystals of the sigmoid and along grain boundaries in the strain shadow and adjacent zones with limited recrystallization. Notably, grain boundaries perpendicular to the main foliation show the most intense CL signals. The layers surrounding the sigmoid contain the smallest grain sizes and are bordered by zones of larger grains.

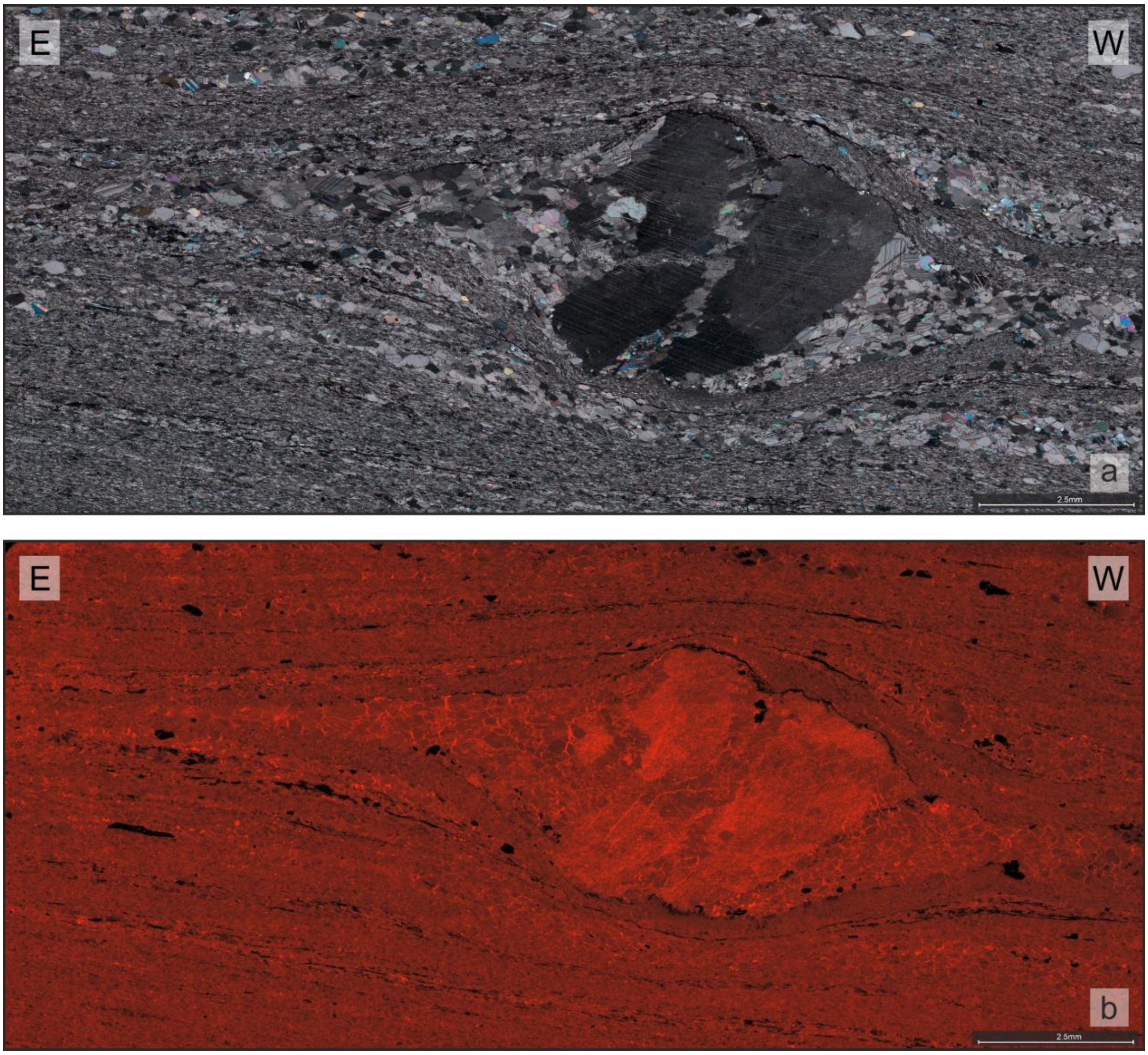

Figure 17: Sample TW04_24 **(a)** XPL- photomosaic of sigmoid in marble ultramylonite showing top to the east ductile shear sense. **(b)** optical CL- photomosaic of sigmoid in Figure 15a taken with an exposure time of 180ms (UTM 33N: 366135/5234950)

The third marble mylonite sample, TW04_23, was collected from a different location near the Penninic–Lower Austroalpine boundary. It displays microstructures similar to the previous samples, with elongated recrystallized calcite grains exhibiting an oblique SPO consistent with top-to-the-east shearing (see Figure 15d). A CL photomosaic of this sample (Figure 18a) shows a generally homogeneous CL signal, with slightly elevated intensity along grain boundaries and in some individual calcite crystals. Stylolites are present parallel to the main foliation (see dark layers in Figure 18b), and the CL image reveals that the highest intensity occurs directly at the stylolites.

In both the marble mylonites and associated metaconglomerates, microstructures related to deformation phase D_1 dominate. Features associated with D_2 and D_3 are also present but are

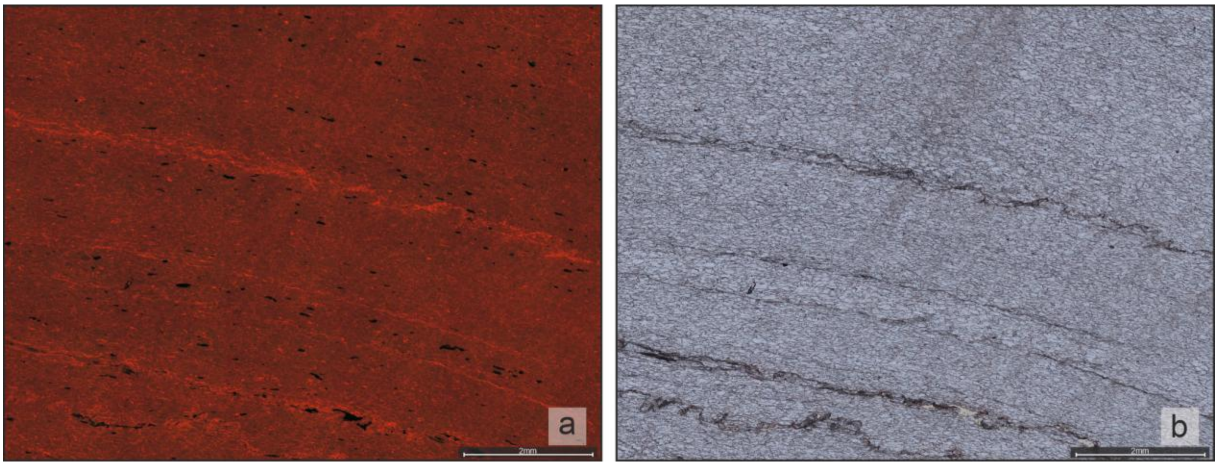

Figure 18: **(a)** optical CL photomosaic of sample TW05_23 showing high CL intensities directly at the stylolites **(b)** PPL photomosaic of the same area showing stylolites in marble mylonite (UTM 33N: 367406/5233908)

difficult to distinguish. In thin sections cut parallel to the XZ axis of the finite strain ellipsoid, D_2 and D_3-related microstructures primarily reflect pressure solution processes. Additional thin sections cut normal to the fold axes of D_2 and D_3 were prepared to examine microscopic folding. In marble mylonites, pressure solution features are best visualized in CL images. Figure 17b for example shows layers and minerals lacking CL signals in the compressive quadrants of the large sigmoid.

Figure 19 presents photomosaics and photomicrographs highlighting pressure solution structures. Sample TW07_23 (Figures 19a, 19c, and 19d), a calc-silicate schist, shows fewer signs of dynamic recrystallization than the previously described mylonites. Calcite and quartz crystals are elongated and exhibit a weak SPO parallel to the main foliation. Twinning in calcite is common but lacks a preferred orientation. Opaque minerals, possibly graphite, accumulate above and below larger grains (Figure 19a). Layers of white mica and graphite, resulting from pressure solution during flattening, are also visible (Figures 19c and 19d). Similar accumulations are observed in metaconglomerates. Figure 19b shows a dolomite component in sample TW12_23 indenting into a white mica and graphite layer formed by pressure solution. Figure 19e displays a marble mylonite with two spaced cleavages (marked “axpl”) of differing orientations, also linked to pressure solution processes.

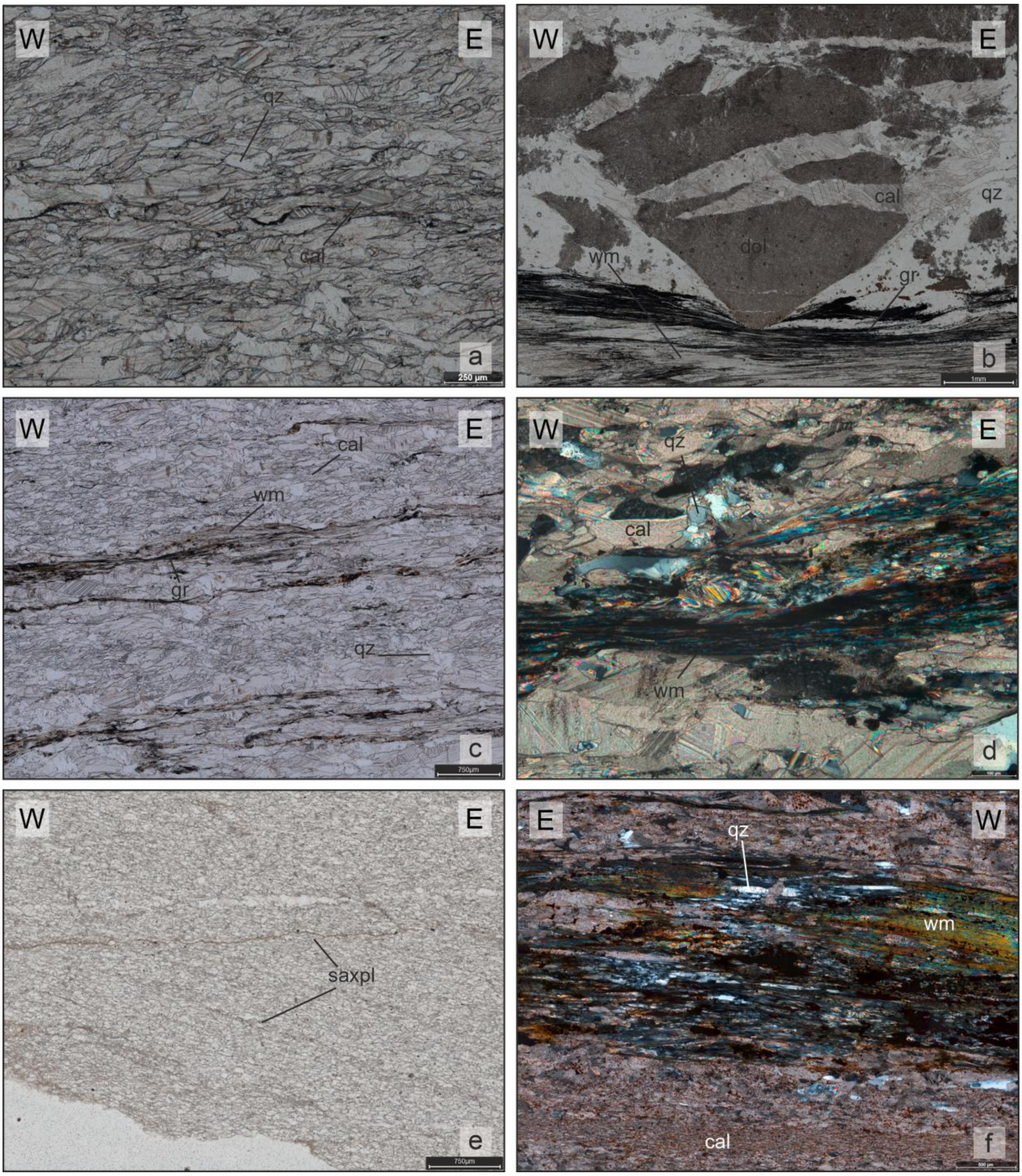

Figure 19**:** Photomicrographs and photomosaics from various samples of the Penninic units showing examples for pressure solution dominated structures. **(a)** PPL- photomicrograph of sample TW07_23 showing signs of pressure solution on the top and bottom grain boundaries of quartz and calcite grains in a meta calc-silicate. The black layer in the middle of the picture is an accumulation of graphite also associated with vertical flattening D$_3$ (UTM33N: 366223/5236749) **(b)** PPL – photomosaic of metaconglomerate (TW12_23) with a dolomite component indenting into a pressure solution dominated layer that is mainly build-up of graphite and white mica. The dolomite component deforms brittle and is crosscut by calcite veins, that do not show signs of dynamic recrystallization (UTM33N: 367308/5233844) **(c)** PPL photomosaic of pressure solution dominated meta calc-silicate schist with layers accumulating graphite and white mica that show vertical flattening as a dominant process. (UTM33N: 366223/5236749) **(d)** White mica and graphite rich layer associated with pressure solution shown in XPL photomosaic of sample TW07_23 (UTM33N: 366223/5236749) **(e)** PPL Photomosaic of calcite mylonite (sample TW05_23) with two different pressure solution schistositys probably associated with the D2 and D3 folding (marked "saxpl") (UTM33N: 367406/5233908) **(f)** XPL photomosaic of sample TW14_23 showing a white mica rich layer that also contains quartz and an opaque mineral (possibly pyrite) accumulated by pressure solution. (UTM33N: 358816/5235288)

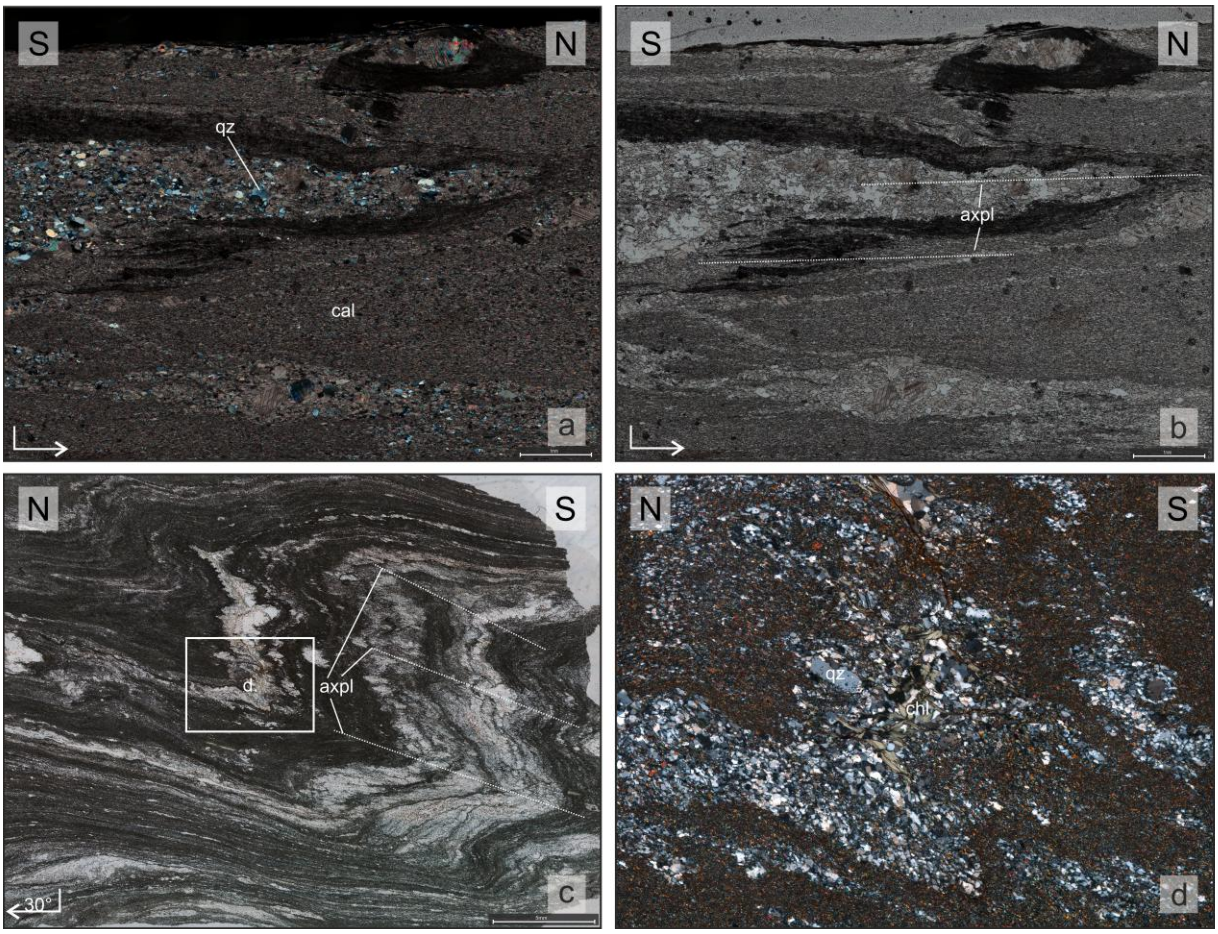

Figure 20: Photomicrographs and photomosaics of thin sections cut parallel to the y-z plane of the finite strain ellipsoid **(a)** XPL photomosaic of a folded meta- calc silicate (TW12_23) (UTM33N: 367308/5233844)**(b)** PPL version of the photomosaic in Fig. 18a with the axial planes of the folds marked with "axpl" (UTM33N: 367308/5233844) **(c)** PPL photomosaic of the whole thin section TW15_02_23 showing a highly folded metabasite. The metabasite consists of interchanging layers of quartz and epidote. The white box marks the location of the photomosaic in Fig.18d. (UTM33N: 369133/5234265) **(d)** Detail photomosaic of folded metabasite. In the fold hinge of the quartz rich layer, chlorite accumulates, partially with its long axis parallel to the axial planes of the folds.

Photomosaics and photomicrographs from thin sections cut normal to the stretching lineation and fold axes are shown in Figure 20. Figures 20a and 20b present XPL and PPL images of folded layers in sample TW12_23, composed mainly of calcite and quartz. Axial planes of the folds marked "axpl" in the PPL image, dip northward, indicating south-verging folds consistent with those described in Chapter 4.2.2. The second set of photomosaics (Figure 20c) shows a highly folded metabasite with alternating quartz-rich and fine-grained epidote-rich layers. Chlorite in the quartz-rich layers is oriented parallel to the axial planes in the fold hinges. When reoriented, these axial planes dip shallowly to the north.

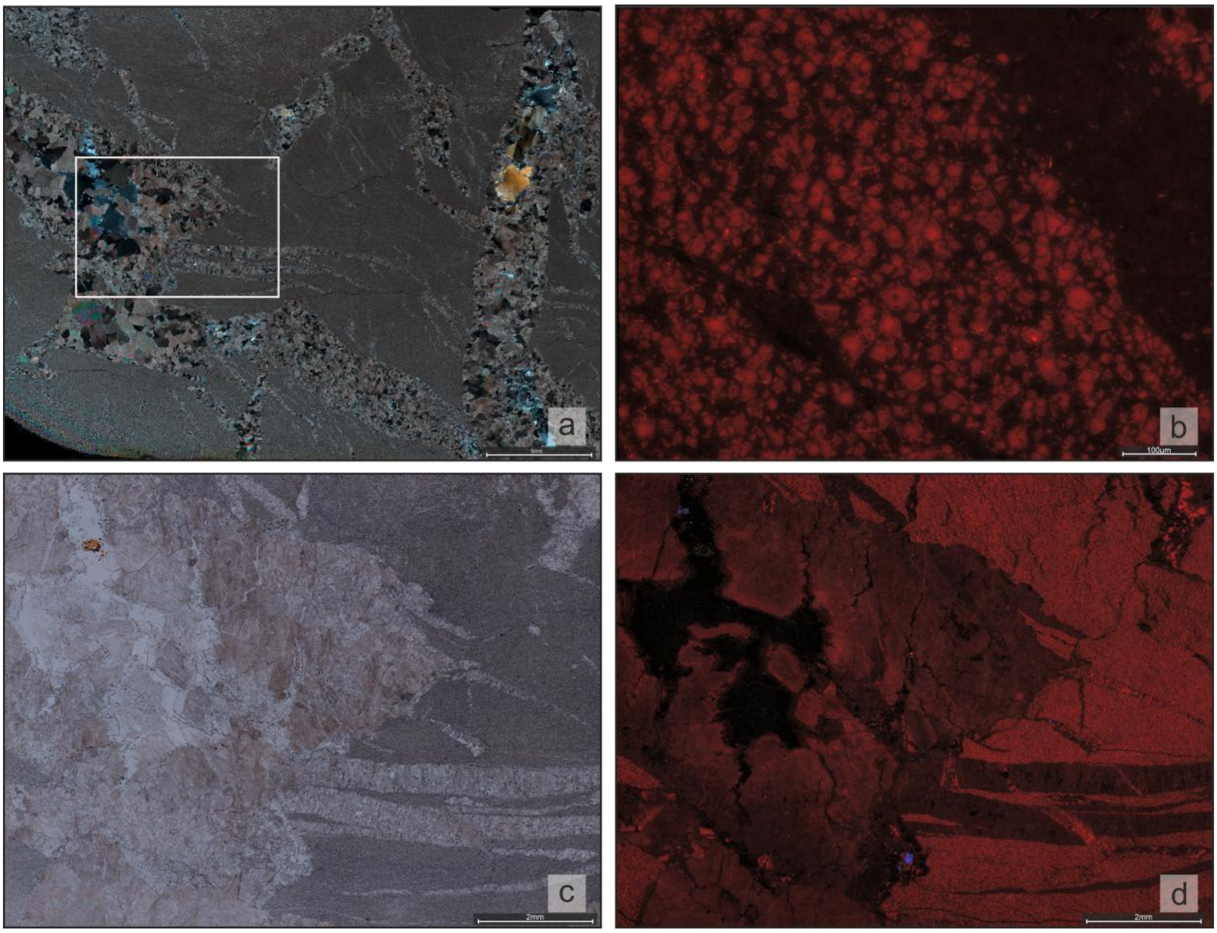

Figure 21: Photomosaics and photomicrographs of sample TW02_23 (UTM 33N: 367125/5233717) The white box in **a** denotes the location of the photomosaics in **c** and **d**

Sample TW02_23, identified as dolomite in the field, occurs in a small area within Penninic rocks and is not attributed to the Lower Austroalpine. It features a fine-grained dolomite matrix crosscut by multiple generations of calcite veins in various orientations. A CL photomosaic and detailed CL images were obtained. In the overview image (Figure 21d), the dolomite matrix shows the highest overall CL intensity, while the crosscutting veins exhibit variable intensities. At higher magnification, individual dolomite crystals display CL zoning, with the lowest intensities at grain boundaries.

In addition to the predominantly Penninic samples, two Lower Austroalpine metagreywacke samples were analysed. These consist mainly of quartz, white mica, and large feldspar clasts. In sample TW03_23 (Figures 22b and 22c), feldspars range from 100–500 µm and are accompanied by white mica strain caps and quartz strain shadows. Their monoclinic symmetry indicates a top-to-the-west ductile shear sense. In sample TW09_23, feldspar clasts are generally larger, reaching up to 1 mm, but show similar structures consistent with top-to-the-west shearing (Figures 22a and 22e). Figure 22d presents a photomicrograph detailing feldspar recrystallization, along with brownish minerals identified as ankerite.

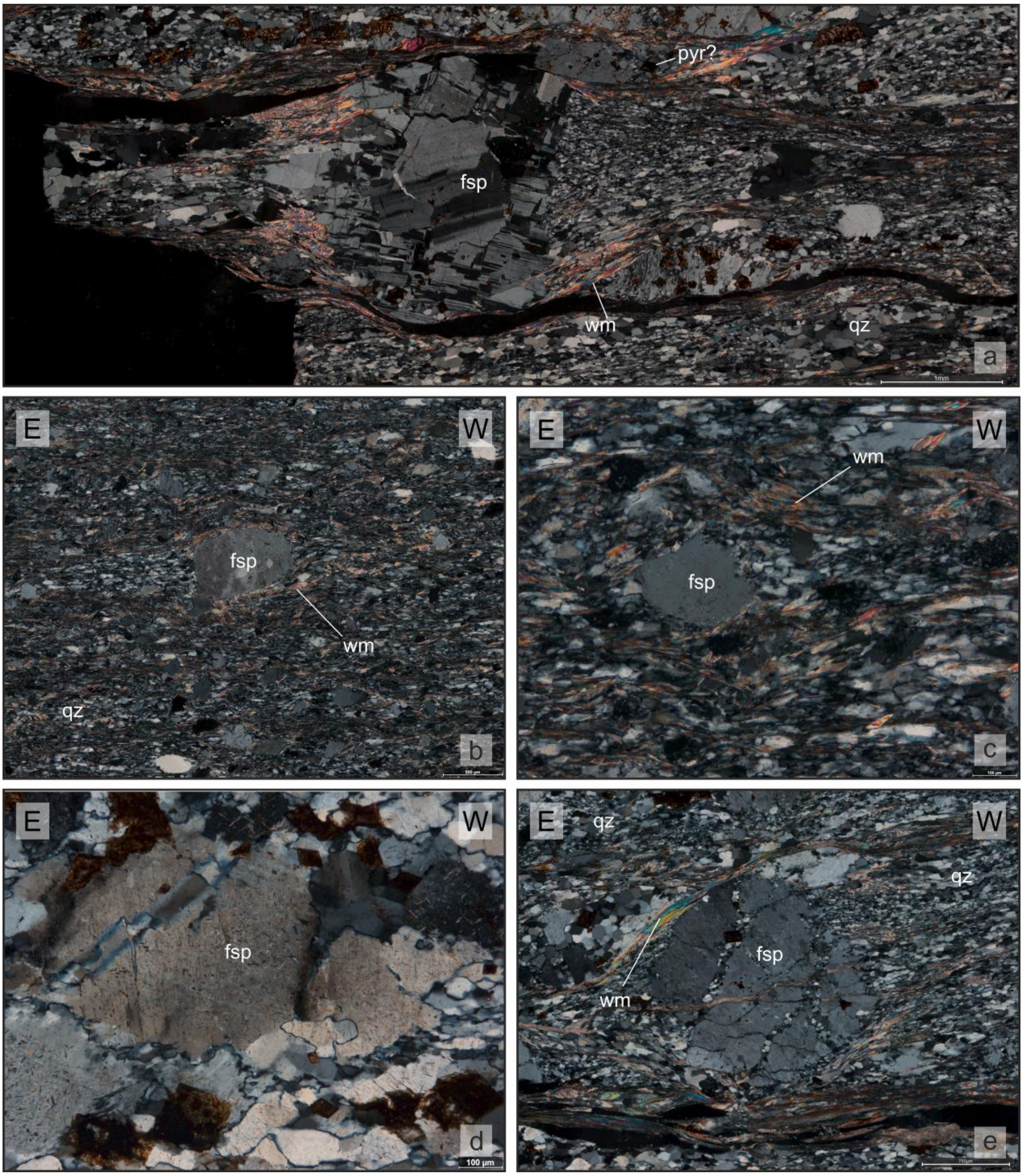

Figure 22: XPL photomosaics and photomicrographs of metagreywacke attributed to the Lower Austroalpine unit in the field. **(a)** large feldspar component in quartzite that shows pinch and swell symmetries with white mica accumulations on the clast matrix boundaries. Brown weathered minerals are ankerite (UTM33N: 365856/5235575) **(b)** feldspar grains in a quartz and white mica matrix show sigmoid shapes, showing top to the west ductile shear senses. (UTM33N: 367159/5233736) **(c)** detail photomicrograph of recrystallizing feldspar in a quartz and white mica matrix showing a slight sigmoid shape with a top to the west ductile shear sense. (UTM33N: 367159/5233736) **(d)** photomicrograph of feldspar dynamically recrystallizing (UTM33N: 365856/5235575) **(e)** dynamically recrystallizing feldspar in sample TW09_23 with sigmoid shape showing top to the west ductile shear sense (UTM33N: 365856/5235575)

4.4 Raman micro- spectroscopy data

Here the results of the Raman micro- spectroscopy are presented and shown on the map.

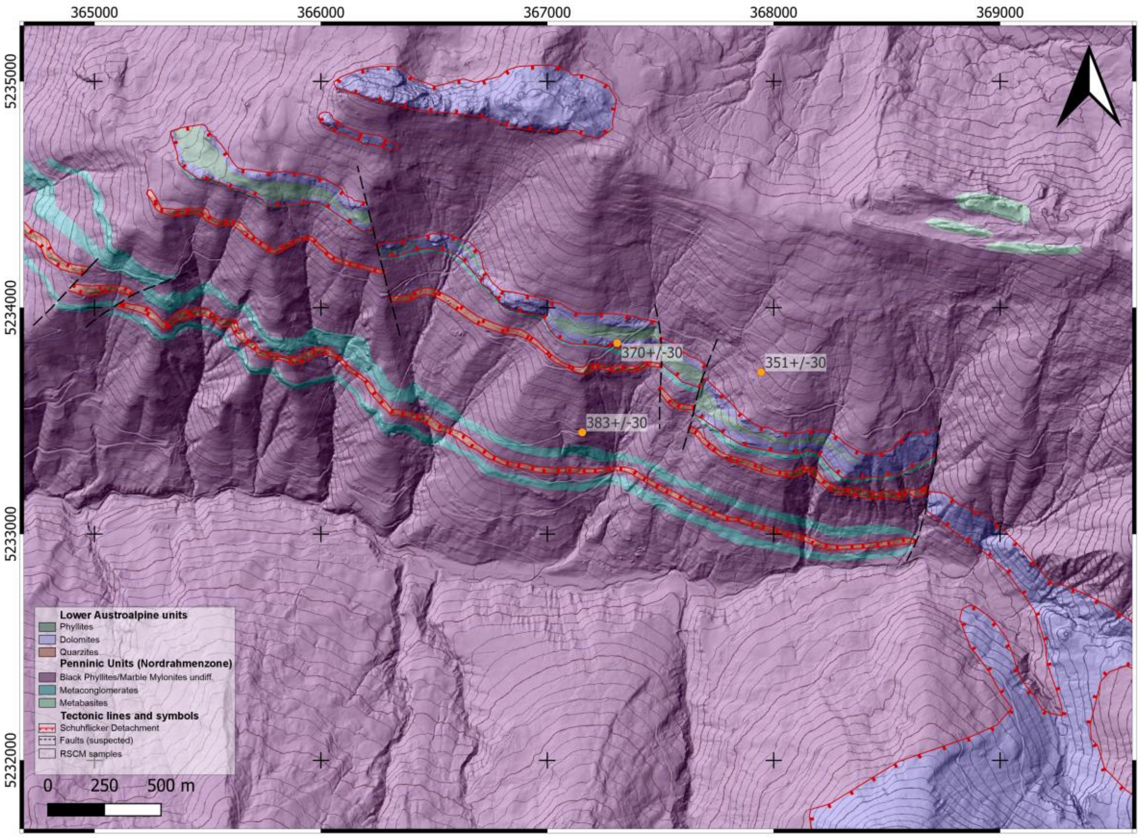

Figure 23:Geologic map of the area around Mt. Saukarkopf with the locations and temperatures of the three RSCM samples

Three graphite bearing samples taken on the eastern profile on the southern flank of Mt. Saukarkopf have been analysed using Raman spectroscopy. All three samples have been taken in units distinguished as Penninic, from which two are graphitic phyllites and one is a graphite bearing metaconglomerate. The results provided by Dr Gerd Rantitsch of the University of Leoben show maximum temperatures during metamorphosis reaching from 351°C to 383°C all within an error of +-30°C. A detailed table of the parameters used to obtain the maximum temperatures using the method of Lünsdorf et al., 2017 can be found in the appendix.

5 Discussion

5.1 Tectonic evolution of the Nordrahmenzone

The data presented in this work reveals the tectonic evolution of the Nordrahmenzone as a complex multi- phase system consisting of four distinguishable stages of deformation D_1-D_4. Because of the lack of minerals suitable for p-T reconstruction with phase diagrams in the lithologies investigated the complete metamorphic conditions cannot be reconstructed. RSCM analyses constrain the peak metamorphic temperatures at a maximum of around 350-400°C. Microstructural observations showing dynamic recrystallization in calcites and quartz and

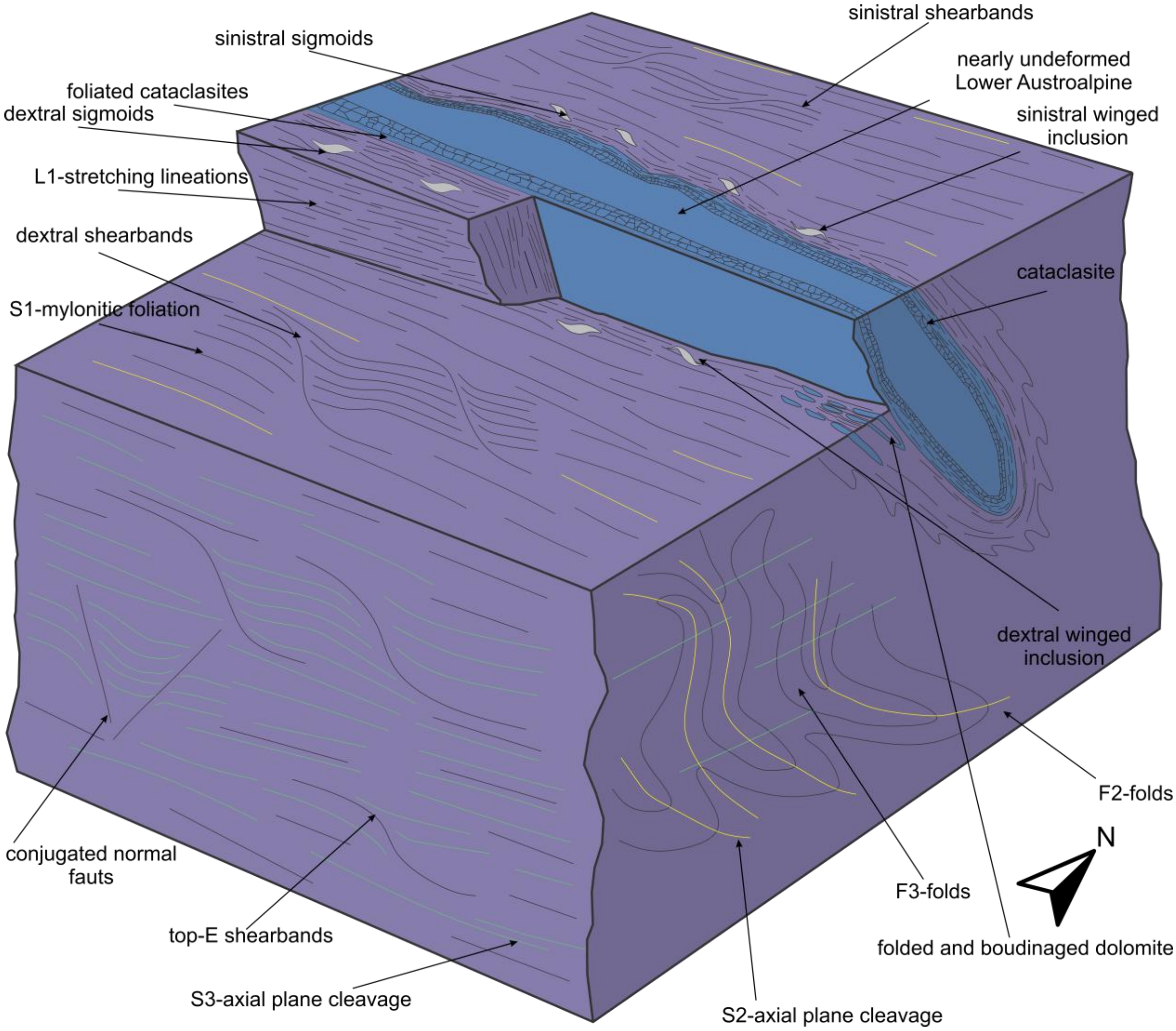

Figure 24: Synoptical 3D-diagram summarizing the structures observed in the study area. Shear deformation in the Peninnic units intensifies towards higher structural levels localizing in a detachment zone of marble ultramylonites and cataclasites. Mylonitic deformation is overprinted by concurrent upright and subhorizontal folding (F2 and F3) with pervasive axial plane cleavages. Everything is overprinted by ongoing top-to- E deformation represented by shearbands and normal faults after folding.

brittle behaviour of dolomite porphyroclasts in metaconglomerates support a temperature around this during deformation.

Within the study area no sedimentary features of the investigated metasediments can be seen, as well as there are no structures pointing to nappe stacking during the subduction of the Penninic oceans.

The first phase of deformation D_1 presents itself as a phase of mylonitization As shown in chapter 4.2.1 the shearing deformation intensifies towards higher structural levels leading to a zone where deformation localizes in highly sheared ultramylonites and cataclasites at the highest structural levels of the Nordrahmenzone directly at the border to the Lower Austroalpine. Within this zone, especially at Mt. Schuhflicker structures like sheath folds, isoclinal folds in the marble mylonites as well as foliated cataclasites in dolomites can be found, that only form under very high strain. The Lower Austroalpine rocks above this zone show no structures that can be attributed to D1 deformation, but structures related to a top to W deformation can be found in meta- greywacke (see Figure 22). Therefore this high strain zone between the Penninic and Lower Austroalpine can be interpreted as major top E detachment, that has first been described and named by Spalding et al., 2025 as *Schuhflicker Detachment*. In the second phase of deformation, that was still active under ductile conditions, N-S shortening led to regional scale folding. The folds show E-W fold axes and a south vergence and fold all units of the Nordrahmenzone as well as the previously described detachment into regional scale syn- and antiforms with subvertical to steeply N dipping fold limbs. Within these large scale synforms the dolomites and quarzites of the Lower Austroalpine are embedded as tectonic klippen within the Penninic metasediments (e.g. Mt. Schuhflicker, Mt. Saukarkopf; see Figure 9). In the upright limbs of these folds, the folded mylonites show an apparent dextral shear sense, in the inverted limbs they show an apparent sinistral shear sense. A pervasive axial plane cleavage of these folds can be found in the field and in thin section too.

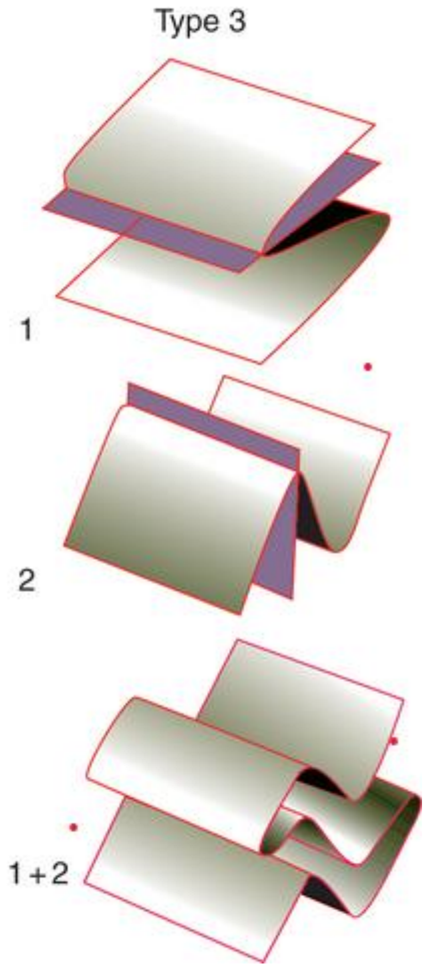

Figure 25: Formation of type 3 refold structures (modified after Fossen, 2016)

The third phase of deformation D_3 led to structures accommodating vertical flattening. The examples for these in the field are shown in chapter 4.2.3 and are mainly open folds with a subhorizontal fold axis as well as a pervasive axial plane cleavage belonging to the fold generation f3. The axial plane cleavage can also be seen in thin section as a spaced pressure solution cleavage. In thin section this phase of generation also is represented by pressure solution rims on the clast matrix boundaries of metaconglomerate components. The interference of this generation of folding with the earlier f2 folds leads to the formation of type 3 refold structures after the classification of Ramsay, 1962 (see Figure 25).

The latest recorded phase of deformation D_4 shows ongoing top to E extensional structures that cut structures related to D_2 and D_3. These structures are mainly the described top to E shearbands, brittle ductile normal faults as well as E-W extensional veins. These structures are still formed under conditions of the brittle-ductile transition zone and record that top E extensional deformation was consecutively and still ongoing after the formation of the structures of D_2 and D_3.

In Figure 24 a synoptical 3D diagram is shown, that summarizes the main features of the structural development in the Nordrahmenzone and at its boundary with the Lower Austroalpine in the hanging wall of the *Schuhflicker Detachment.*

5.2 Role of the SEMP for ductile shearing

The Salzachtal- Ennstal- Mariazell Puchberg (SEMP) Fault is one of the most important strike slip faults for lateral extrusion during the Miocene in the Eastern Alps (e.g. Decker & Peresson, 1996; Linzer et al., 2002; Ratschbacher et al., 1991). The SEMP represents the northern border of the eastern Tauern Window and juxtaposes the units of the Nordrahmenzone in the south to the Austroalpine superunit in the north. In previous work it has been described, that the subvertical mylonites of the northern part of the Nordrahmenzone (i.e. Klammkalkzone) represent the exhumed ductile shearzone of the sinistral SEMP (e.g. Frost et al., 2011; Wang & Neubauer, 1998). Towards the west Rosenberg & Schneider, 2008 suggest, that the termination of the SEMP is a sinistral mylonitic shear zone, that goes into the western gneiss core of the Tauern Window and changes deformation of the SEMP from a purely sinistral to a more transpressional character (i.e. Ahorn shear zone).

Figure 26: Fault gouge of the SEMP fault at the entrance of the Liechtensteinklamm. Picture taken looking south. (UTM33N: 363326/5241671)

As discussed before, the mylonites of the Nordrahmenzone formed due to a major detachment and have been folded by a second generation of deformation into regional scale upright folds. Because of this folding a large part of the mylonites of the Nordrahmenzone are subvertical and show apparent strike slip shear senses that change kinematic when changing fold limbs. The ductile structures described by Frost et al., 2011; and Wang & Neubauer, 1998 are similar to the ductile features described in this work, that clearly belong to the top to E Schuhflicker detachment, that affected the whole Nordrahmenzone. Therefore, we suggest that the mylonites previously described as the exhumed ductile shear zone of the SEMP rather represent the inverted limb of a regional scale f2 fold. The only structures found at the Northern contact between the Nordrahmenzone and the Austroalpine superunit that can be clearly attributed to the SEMP fault are of a brittle character like for example a thick grey fault gauge that can be seen at the entrance of the Liechtensteinklamm (see Figure 26). We therefore also suggest that the SEMP, at least from the Nordrahmenzone onwards to the east, represents an upper crustal, purely brittle fault, that does not have a ductile root. The western termination of the SEMP in the Ahorn shear zone shows quite a similar deformational character with steep dipping mylonites showing strike slip shear senses and also upright folding similar to the f2 folds in the Nordrahmenzone (Rosenberg & Schneider, 2008). In respect to this and the interpretation that the SEMP in the east does not go to deeper crustal levels, the question arises, if the interpretation of the Ahorn shear zone as the western termination of the SEMP is still valid, so doing more work there with this perspective might bring new models for the evolution of the SEMP and the Ahorn shear zone.

5.3 Schuhflicker Detachment and Katschberg Normal Fault

At the eastern border of the Tauern window, the Katschberg Normal Fault (KNF) is widely recognized as the major low angle normal fault accommodating a high amount of exhumation of the Peninnic and Sub- Penninic units of the Tauern Window. Previous studies have shown that the activity of the KNF started at around 21Ma (Wolff et al., 2024) and accommodated about 23-26km of orogen parallel extension during the Miocene (Scharf et al., 2013). The study of Spalding et al., 2025, that first described the Schuhflicker Detachment presents white mica $^{40}Ar/^{39}Ar$ ages of around 30 Ma, that they interpret to be ages representing the onset of ductile deformation at the detachment pre- dating the activity of the KNF. Older studies also report white mica $^{40}Ar/^{39}Ar$ ages of 30 Ma on samples taken from the border between the Matrei-Nordrahmenzone nappe system, that support the earlier onset of deformation at the Schuhflicker Detachment than at the KNF (Liu et al., 2001). These ages suggest that the Schuhflicker Detachment represents an earlier phase of E-W extension that pre dates the Miocene exhumation along the Katschberg and Brenner Normal Faults and therefore the indentation of the Dolomites Indenter that is dated to be concurrent with the onset of deformation at the Katschberg Normal Fault (Ratschbacher et al., 1991; Scharf et al., 2013). It therefore represents the earliest phase of E-W extension and exhumation in the Tauern Window, that later in the Miocene moved to the Katschberg normal fault.

The timing of deformation onset at the Schuhflicker Detachment coincides with the age of formation and exhumation of the eclogites of the Eclogite zone (Gleissner et al., 2007; Glodny et al., 2005; Smye et al., 2011; Zimmermann et al., 1994), showing that in the Tauern Window E-W extension and exhumation in the middle to upper crust happened concurrently with the decompression of the high-pressure units along the subducting slab and N-S shortening.

6 Conclusions

The new data presented in this work gives an insight into the earliest phase of E- W extension in the eastern Tauern Window. The fieldwork carried out around Mt. Saukarkopf and Mt. Schuhflicker, and the microstructural observation show a complex tectonic evolution with 4 concurrent deformation phases showing an interplay of mylonitic top to E shearing (D_1) N-S shortening (D_2), vertical flattening (D_3) and late-stage brittle ductile E-W extension (D_4). The mylonitic deformation in the Nordrahmenzone is caused by a major top to E detachment (Schuhflicker Detachment) that localizes at the boundary between the Matrei Nordrahmenzone nappe system and the Lower Austroalpine nappe system in highly deformed ultramylonites and cataclasites. Raman Spectroscopy of Carbonaceous Material reveals that the mylonitization operated under peak temperatures of around 350-400° C. The Schuhflicker Detachment represents the earliest phase of E-W extension, starting during the Oligocene with top to E deformation moving to the Katschberg normal fault in the Miocene. Due to large scale D2 folding the mylonites are folded into syn- and antiforms with sub- vertical fold limbs. Within the synforms the Lower Austroalpine units are exposed as tectonic klippen. We interpret the sub- vertical mylonites as mylonites belonging to the Schuhflicker Detachment rather than previous studies, that attributed them to the sinistral SEMP fault. Therefore, we suggest that the SEMP does not have a ductile part and is a purely brittle strike-slip fault.

7 References

Behrmann, J. H. (1988). Crustal-scale extension in a convergent orogen: The Sterzing-Steinach mylomte zone in the Eastern Alps. *Geodinamica Acta*, *2*(2), 63–73. https://doi.org/10.1080/09853111.1988.11105157

Decker, Kurt, & Peresson, H. (1996). *Tertiary kinematics in the Alpine-Carpathian-Pannonian system: Links between thrusting, transform faulting and crustal extension*.

Frisch, W. (1979). Tectonic progradation and plate tectonic evolution of the Alps. *Tectonophysics*, *60*(3–4), 121–139. https://doi.org/10.1016/0040-1951(79)90155-0

Frisch, W., Dunkl, I., & Kuhlemann, J. (2000). Post-collisional orogen-parallel large-scale extension in the Eastern Alps. *Tectonophysics*, *327*(3), 239–265. https://doi.org/10.1016/S0040-1951(00)00204-3

Froitzheim, N., Plašienka, D., & Schuster, R. (2008). Alpine tectonics of the Alps and Western Carpathians. In *The geology of Central Europe* (pp. 1141–1232). Geological Society (London).

Frost, E., Dolan, J., Ratschbacher, L., Hacker, B., & Seward, G. (2011). Direct observation of fault zone structure at the brittle-ductile transition along the Salzach-Ennstal-Mariazell-Puchberg fault system, Austrian Alps. *Journal of Geophysical Research: Solid Earth*, *116*(B2). https://doi.org/10.1029/2010JB007719

Fügenschuh, B., Seward, D., & Mancktelow, N. (1997). Exhumation in a convergent orogen: The western Tauern window. *Terra Nova*, *9*, 213–217. https://doi.org/10.1111/j.1365-3121.1997.tb00015.x

Genser, J., & Neubauer, F. (1989). Low angle normal faults at the eastern margin of the Tauern Window (Eastern Alps). *Mitteilungen Der Österreichische Geologische Gesellschaft*, *81*, 233–243.

Gleissner, P., Glodny, J., & Franz, G. (2007). Rb-Sr isotopic dating of pseudomorphs after lawsonite in metabasalts from the Glockner nappe, Tauern Window, Eastern Alps. *European Journal of Mineralogy*, *19*(5), 723–734. https://doi.org/10.1127/0935-1221/2007/0019-1755

Glodny, J., Ring, U., Kühn, A., Gleissner, P., & Franz, G. (2005). Crystallization and very rapid exhumation of the youngest Alpine eclogites (Tauern Window, Eastern Alps) from Rb/Sr mineral assemblage analysis. *Contributions to Mineralogy and Petrology*, *149*(6), 699–712. https://doi.org/10.1007/s00410-005-0676-5

Kurz, W., Handler, R., & Bertoldi, C. (2008). Tracing the exhumation of the Eclogite Zone (Tauern Window, Eastern Alps) by 40Ar/39Ar dating of white mica in eclogites. In N. Froitzheim & S. M. Schmid (Eds.), *Orogenic Processes in the Alpine Collision Zone* (pp. S191–S206). Birkhäuser Basel.

Kurz, W., & Neubauer, F. (1996). Deformation partitioning during updoming of the Sonnblick area in the Tauern Window (Eastern Alps, Austria). *Journal of Structural Geology*, *18*(11), 1327–1343. https://doi.org/10.1016/S0191-8141(96)00057-0

Linzer, H.-G., Decker, K., Peresson, H., Dell'Mour, R., & Frisch, W. (2002). Balancing lateral orogenic float of the Eastern Alps. *Tectonophysics*, *354*(3), 211–237. https://doi.org/10.1016/S0040-1951(02)00337-2

Liu, Y., Genser, J., Handler, R., Friedl, G., & Neubauer, F. (2001). 40Ar/39Ar muscovite ages from the Penninic-Austroalpine plate boundary, Eastern Alps. *Tectonics*, *20*(4), 526–547. https://doi.org/10.1029/2001TC900011

Lünsdorf, N. K., Dunkl, I., Schmidt, B. C., Rantitsch, G., & Von Eynatten, H. (2017). Towards a Higher Comparability of Geothermometric Data Obtained by Raman Spectroscopy of Carbonaceous Material. Part 2: A Revised Geothermometer. *Geostandards and Geoanalytical Research*, *41*(4), Article 4. https://doi.org/10.1111/ggr.12178

Peer, H., & Zimmer, W. (1980). Geologie der Nordrahmenzone der Hohen Tauern (Gasteiner Ache bis Saukarkopf-Großarltal). *Jahrbuch der Geologischen Bundesanstalt*, *123*(2), 411–466.

Peer, & Zimmer. (1977). *Geologische Karte der Nordrahmenzone der Hohen Tauern zwischen Gasteinertal und östlichem Großarltal (Saukarkopf), Salzburg* [Geological map]. Geologische Bundesanstalt.

Ramsay, J. G. (1962). Interference Patterns Produced by the Superposition of Folds of Similar Type. *The Journal of Geology*, *70*(4), 466–481. https://doi.org/10.1086/626837

Rantitsch, G. (2023). Graphite thermometry by interactive fitting of Raman spectra. *International Journal of Coal Geology*, *271*, 104232. https://doi.org/10.1016/j.coal.2023.104232

Rantitsch, G., Grogger, W., Teichert, C., Ebner, F., Hofer, C., Maurer, E.-M., Schaffer, B., & Toth, M. (2004). Conversion of carbonaceous material to graphite within the Greywacke Zone of the Eastern Alps. *International Journal of Earth Sciences*, *93*, 959–973. https://doi.org/10.1007/s0053%25201-004-0436-1

Ratschbacher, L., Frisch, W., Linzer, H., & Merle, O. (1991). Lateral extrusion in the eastern Alps, Part 2: Structural analysis. *Tectonics*, *10*(2), 257–271. https://doi.org/10.1029/90TC02623

Rosenberg, C. L., & Garcia, S. (2011). Estimating displacement along the Brenner Fault and orogen-parallel extension in the Eastern Alps. *International Journal of Earth Sciences*, *100*(5), 1129–1145. https://doi.org/10.1007/s00531-011-0645-3

Rosenberg, C. L., & Schneider, S. (2008). The western termination of the SEMP Fault (eastern Alps) and its bearing on the exhumation of the Tauern Window. *Geological Society, London, Special Publications*, *298*(1), 197–218. https://doi.org/10.1144/SP298.10

Scharf, A., Handy, M. R., Favaro, S., Schmid, S. M., & Bertrand, A. (2013). Modes of orogen-parallel stretching and extensional exhumation in response to microplate indentation and roll-back subduction (Tauern Window, Eastern Alps). *International Journal of Earth Sciences*, *102*(6), 1627–1654. https://doi.org/10.1007/s00531-013-0894-4

Schmid, S. M., Fügenschuh, B., Kissling, E., & Schuster, R. (2004). Tectonic map and overall architecture of the Alpine orogen. *Eclogae Geologicae Helvetiae*, *97*, 93–117. https://doi.org/10.1007/s00015-004-1113-x

Schmid, S. M., Scharf, A., Handy, M. R., & Rosenberg, C. L. (2013). The Tauern Window (Eastern Alps, Austria): A new tectonic map, with cross-sections and a tectonometamorphic synthesis. *Swiss Journal of Geosciences*, *106*, 1–32. https://doi.org/10.1007/s00015-013-0123-y

Schuster, R., & Stüwe, K. (2022). Geological and Tectonic Setting of Austria. In C. Embleton-Hamann (Ed.), *Landscapes and Landforms of Austria* (pp. 3–26). Springer International Publishing. https://doi.org/10.1007/978-3-030-92815-5_1

Selverstone, J. (1988). Evidence for east-west crustal extension in the Eastern Alps: Implications for the unroofing history of the Tauern window. *Tectonics*, *7*(1), 87–105. https://doi.org/10.1029/TC007i001p00087

Smye, A. J., Bickle, M. J., Holland, T. J. B., Parrish, R. R., & Condon, D. J. (2011). Rapid formation and exhumation of the youngest Alpine eclogites: A thermal conundrum to Barrovian metamorphism. *Earth and Planetary Science Letters*, *306*(3), 193–204. https://doi.org/10.1016/j.epsl.2011.03.037

Spalding, J., Schneider, D., Huet, B., Grasemann, B., & Rantitsch, G. (2025). East Tauern Detachment System: Coupled Oligocene Ductile Thinning and Miocene Extension of the Eastern European Alps. *Tectonics*, *44*(5), e2024TC008800. https://doi.org/10.1029/2024TC008800

Tricart, P. (1984). From passive margin to continental collision; a tectonic scenario for the Western Alps. *American Journal of Science*, *284*(2), 97–120. https://doi.org/10.2475/ajs.284.2.97

Wang, X., & Neubauer, F. (1998). Orogen-parallel strike-slip faults bordering metamorphic core complexes: The Salzach–Enns fault zone in the Eastern Alps, Austria. *Journal of Structural Geology*, *20*(6), 799–818. https://doi.org/10.1016/S0191-8141(98)00013-3

Wiederkehr, M., Bousquet, R., Schmid, S. M., & Berger, A. (2008). From subduction to collision: Thermal overprint of HP/LT meta-sediments in the north-eastern Lepontine Dome (Swiss Alps) and consequences regarding the tectono-metamorphic evolution of the Alpine orogenic wedge. *Swiss Journal of Geosciences*, *101*(1), 127–155. https://doi.org/10.1007/s00015-008-1289-6

Wolff, R., Wölfler, A., Hampel, A., & Dunkl, I. (2024). Constraining the slip history of the Katschberg normal fault (Eastern Tauern Window) by thermo-kinematic modeling: Implications for the tectonic evolution of the Eastern European Alps in the late Cenozoic. *Tectonophysics*, *890*, 230514. https://doi.org/10.1016/j.tecto.2024.230514

Zimmermann, R., Hammerschmidt, K., & Franz, G. (1994). Eocene high pressure metamorphism in the Penninic units of the Tauern Window (Eastern Alps): Evidence from40Ar−39Ar dating and petrological investigations. *Contributions to Mineralogy and Petrology*, *117*(2), 175–186. https://doi.org/10.1007/BF00286841

8 List of figures

9 Appendix

9.1 Table of measurements

Locality	latitude	longitude	Type	dip direction	dip
Locality 02	47.24666	13.2131212	l1	97	3
Locality 02	47.246614	13.2131229	l1	272	9
Locality 02	47.246622	13.2131259	l1	274	10
Locality 02	47.246554	13.2131586	s	333	21
Locality 02	47.246597	13.2131174	s	343	11
Locality 02	47.246602	13.2131192	s	344	25
Locality 02	47.246604	13.2131184	s	337	21
Locality 02	47.246654	13.2131329	s	349	28
Locality 02	47.246657	13.2131515	s	16	18
Locality 02	47.246647	13.213145	s	20	19
Locality 02	47.246643	13.2131305	s	9	25
Locality 02	47.246538	13.2130594	s	318	11
Locality 02	47.246538	13.2130594	s	300	26
Locality 02	47.246538	13.2130594	s	39	33
Locality 02	47.246538	13.2130594	l1	282	5
Locality 02	47.246538	13.2130594	l1	286	15
Locality 02	47.246653	13.2131221	l1	287	2
Locality 02	47.246538	13.2130594	l1	294	0
Locality 03	47.238582	13.1934784	s	209	76
Locality 03	47.247216	13.2133266	s	12	70
Locality 03	47.247211	13.213327	s	12	60
Locality 03	47.247211	13.2133269	s	350	79
Locality 03	47.247209	13.2133508	axpl3	218	25
Locality 03	47.247216	13.2133344	axpl3	203	19
Locality 03	47.247243	13.2133252	s	277	83
Locality 03	47.247244	13.213326	s	265	84
Locality 03	47.247244	13.2133252	s	27	85
Locality 03	47.24722	13.2133184	l1	302	15
Locality 03	47.247223	13.2133162	l1	292	10
Locality 03	47.247187	13.21337	fa2	128	0
Locality 03	47.247201	13.2133711	fa3	126	7
Locality 03	47.247196	13.2132905	l1	306	7
Locality 03	47.247203	13.2132969	l1	304	9
Locality 03	47.247219	13.213312	l1	299	8
Locality 04	47.246538	13.2130594	s	333	41
Locality 04	47.246538	13.2130594	s	331	41
Locality 05	47.247144	13.2133445	s	20	44

Locality 05	47.247148	13.2133534	l1	110	1
Locality 06	47.246041	13.2156481	s	4	70
Locality 06	47.246036	13.2156519	s	350	62
Locality 06	47.246044	13.2156444	l1	297	30
Locality 07	47.24616	13.2159378	s	323	60
Locality 07	47.246171	13.215915	s	355	55
Locality 07	47.246138	13.2158262	s	3	67
Locality 07	47.24614	13.2158221	l1	286	9
Locality 07	47.246138	13.2158292	l1	289	11
Locality 09	47.247028	13.2169121	s	289	27
Locality 09	47.247028	13.2169057	s	278	29
Locality 09	47.247022	13.216871	s	316	36
Locality 09	47.24701	13.2169414	s	332	49
Locality 09	47.247046	13.2168884	l1	274	25
Locality 09	47.247054	13.216902	l1	287	30
Locality 10	47.246803	13.2197939	s	308	20
Locality 10	47.246756	13.2198163	s	303	21
Locality 10	47.246796	13.2198403	s	330	28
Locality 10	47.2467	13.2200437	s	11	16
Locality 10	47.246757	13.2202423	axpl3	0	28
Locality 10	47.246765	13.2202334	s	146	84
Locality 10	47.246764	13.2202206	s	235	17
Locality 10	47.246745	13.2201674	s	11	37
Locality 10	47.246737	13.2201676	s	13	28
Locality 10	47.246757	13.2202503	fa2	297	12
Locality 10	47.246799	13.2197911	l1	267	17
Locality 10	47.24679	13.2198118	l1	285	16
Locality 10	47.246758	13.2202567	l1	290	13
Locality 11	47.246701	13.2148049	s	352	23
Locality 11	47.246765	13.2147642	axpl3	357	24
Locality 11	47.24676	13.2147868	s	3	39
Locality 11	47.246767	13.2147767	fa2	295	2
Locality 11	47.24677	13.2147806	l1	280	10
Locality 12	47.246293	13.214908	s	342	32
Locality 12	47.246293	13.214908	s	348	36
Locality 12	47.246293	13.214908	s	349	32
Locality 12	47.246293	13.214908	s	7	34
Locality 12	47.246293	13.214908	l1	279	15
Locality 13	47.246293	13.214908	s	212	88
Locality 13	47.246293	13.214908	s	341	89
Locality 13	47.246293	13.214908	s	17	71
Locality 13	47.246293	13.214908	s	114	88
Locality 13	47.246293	13.214908	s	255	64
Locality 13	47.246293	13.214908	s	230	57
Locality 13	47.246293	13.214908	s	282	90

Locality 13	47.246293	13.214908	s	255	85
Locality 13	47.246293	13.214908	s	241	73
Locality 13	47.246293	13.214908	s	248	83
Locality 13	47.246293	13.214908	s	231	69
Locality 13	47.254193	13.2316657	l1	112	13
Locality 13	47.246293	13.214908	l1	357	11
Locality 13	47.246293	13.214908	l1	95	3
Locality 13	47.246293	13.214908	l1	336	14
Locality 14	47.254192	13.2314215	s	11	57
Locality 14	47.254199	13.2314328	s	358	70
Locality 14	47.254183	13.2314409	s	305	88
Locality 14	47.254125	13.231414	s	217	84
Locality 14	47.25412	13.2314053	s	213	74
Locality 14	47.254162	13.2313839	s	134	87
Locality 14	47.25416	13.2313899	s	187	90
Locality 14	47.254161	13.2314142	s	11	71
Locality 14	47.254121	13.2313879	l1	126	2
Locality 15	47.254371	13.2307749	s	222	74
Locality 15	47.254373	13.230774	s	243	74
Locality 15	47.254374	13.2307786	s	237	76
Locality 15	47.254371	13.230778	s	30	87
Locality 15	47.254372	13.2307723	l1	113	6
Locality 15	47.254373	13.2307718	l1	118	8
Locality 15	47.254376	13.2307719	l1	120	10
Locality 17	47.252301	13.2228552	s	0	19
Locality 17	47.252309	13.2228668	s	3	19
Locality 18	47.251364	13.221624	s	35	77
Locality 18	47.251346	13.2216353	s	44	74
Locality 18	47.251339	13.2216569	s	62	74
Locality 18	47.251399	13.2216036	l1	179	18
Locality 18	47.251397	13.2216029	l1	330	6
Locality 19	47.251281	13.2209375	s	15	59
Locality 19	47.251282	13.2209366	s	12	64
Locality 19	47.251275	13.2209468	l1	299	3
Locality 19	47.251277	13.2209408	l1	301	0
Locality 20	47.251025	13.2214834	s	223	64
Locality 20	47.251025	13.2214834	s	29	44
Locality 20	47.251025	13.2214834	l1	115	8
Locality 20	47.251025	13.2214834	l1	114	8
Locality 21	47.25082	13.2216302	shearband	71	28
Locality 21	47.250819	13.22166	shearband	84	41
Locality 22	47.250764	13.2219887	s	14	55
Locality 22	47.250766	13.2219923	s	15	55
Locality 22	47.250766	13.2219928	s	13	66
Locality 22	47.250762	13.2219929	s	20	63

Locality 23	47.250538	13.2234661	s	354	43
Locality 23	47.250536	13.2234608	s	338	32
Locality 23	47.250541	13.2234663	s	338	36
Locality 23	47.250537	13.2234694	s	349	48
Locality 24	47.250359	13.224329	shearband	113	28
Locality 24	47.250351	13.2243162	shearband	91	26
Locality 24	47.250349	13.2243174	shearband	105	31
Locality 24	47.250335	13.22431	s	4	24
Locality 24	47.250324	13.2243038	s	338	35
Locality 24	47.250306	13.2243	s	253	38
Locality 25	47.247689	13.2230237	shearband	1	17
Locality 25	47.247692	13.2230508	s	297	29
Locality 25	47.247693	13.2230499	s	300	21
Locality 26	47.274456	13.2306936	Fault	1	60
Locality 26	47.274456	13.2306936	Fault	356	56
Locality 26	47.274456	13.2306936	s	168	16
Locality 26	47.274456	13.2306936	s	197	30
Locality 26	47.274456	13.2306936	s	176	43
Locality 26	47.274495	13.2308944	s	175	19
Locality 26	47.274501	13.2309233	s	192	17
Locality 26	47.274511	13.2309206	s	182	9
Locality 26	47.274456	13.2306936	Slickenside	339	58
Locality 26	47.274456	13.2306936	Slickenside	351	54
Locality 26	47.274456	13.2306936	l1	284	6
Locality 26	47.274523	13.2309186	l1	85	1
Locality 27	47.270504	13.2313776	s	345	33
Locality 28	47.267077	13.2260757	axpl3	350	28
Locality 28	47.267075	13.2260551	s	187	34
Locality 28	47.267067	13.2260496	s	184	16
Locality 28	47.267071	13.2260404	s	207	51
Locality 28	47.267095	13.2261139	s	358	34
Locality 28	47.26708	13.226083	fa2	278	24
Locality 28	47.267077	13.2260428	l1	292	23
Locality 28	47.267079	13.2260391	l1	283	10
Locality 29	47.266585	13.2256811	s	2	4
Locality 29	47.266582	13.2256496	s	68	6
Locality 29	47.266628	13.2256896	s	0	1
Locality 29	47.266575	13.2257065	l1	97	3
Locality 29	47.266583	13.2257081	l1	92	1
Locality 30	47.260029	13.2269468	s	24	23
Locality 30	47.260005	13.2269364	s	9	69
Locality 30	47.260026	13.2269355	s	21	36
Locality 30	47.260025	13.2269369	s	27	26
Locality 30	47.260027	13.2269409	s	28	26
Locality 30	47.264895	13.2316219	shearband	196	17

Locality 30	47.264936	13.2316396	shearband	197	21
Locality 30	47.264896	13.2317014	shearband	259	27
Locality 30	47.264849	13.231676	s	246	25
Locality 30	47.264951	13.231721	l1	284	13
Locality 32	47.241415	13.2091287	s	336	26
Locality 32	47.24142	13.2091269	s	342	49
Locality 32	47.241419	13.2091231	s	347	33
Locality 32	47.241412	13.2091051	l1	256	15
Locality 32	47.241414	13.2091113	l1	240	16
Locality 32	47.24141	13.209135	l1	74	0
Locality 33	47.241476	13.2119295	s	2	47
Locality 33	47.241481	13.2119364	s	1	45
Locality 33	47.241566	13.2104538	s	322	49
Locality 33	47.241582	13.2104353	s	325	29
Locality 33	47.24159	13.2104129	s	345	44
Locality 33	47.241639	13.2105061	shearband	33	25
Locality 33	47.241551	13.210242	s	338	50
Locality 33	47.241557	13.2102382	s	7	39
Locality 33	47.241533	13.2101604	s	358	37
Locality 33	47.241545	13.2101726	s	347	30
Locality 33	47.241546	13.2101712	s	9	26
Locality 33	47.241547	13.2101709	s	1	35
Locality 33	47.241546	13.2101704	s	332	36
Locality 33	47.241546	13.2101713	s	2	40
Locality 33	47.241481	13.2119354	fa3	272	13
Locality 33	47.241474	13.2119368	fa3	270	7
Locality 33	47.24147	13.2119344	l1	281	6
Locality 33	47.241584	13.2104495	l1	274	27
Locality 33	47.24154	13.2102368	l1	279	24
Locality 33	47.241531	13.2101468	l1	81	14
Locality 33	47.24153	13.2101477	l1	59	11
Locality 33	47.241527	13.210157	l1	85	11
Locality 34	47.241194	13.244674	s	14	71
Locality 34	47.241192	13.2446826	l1	291	18
Locality 35	47.245024	13.2392637	Fault	109	49
Locality 35	47.244991	13.2392464	Fault	321	48
Locality 37	47.245537	13.249233	s	155	11
Locality 37	47.245611	13.2491843	s	78	9
Locality 37	47.24527	13.2478616	s	29	44
Locality 37	47.245183	13.2475566	axpl3	202	20
Locality 37	47.245151	13.2474385	s	204	49
Locality 37	47.245178	13.2474376	s	206	53
Locality 37	47.245535	13.2492026	l1	86	5
Locality 37	47.245178	13.2475653	fa3	10	5
Locality 37	47.245147	13.2474348	l1	100	10

Locality 37	47.245147	13.2474352	l1	118	17
Locality 38	47.244171	13.253067	s	24	16
Locality 38	47.244171	13.253073	s	18	21
Locality 38	47.244192	13.2530526	l1	291	6
Locality 38	47.244185	13.2530579	l1	287	3
Locality 39	47.243615	13.2550987	s	36	29
Locality 39	47.243632	13.2550764	l1	291	2
Locality 40	47.245341	13.2536215	s	25	12
Locality 40	47.245341	13.2536215	s	345	11
Locality 40	47.245341	13.2536215	s	87	31
Locality 40	47.245341	13.2536215	l1	255	6
Locality 40	47.245341	13.2536215	l1	121	15
Locality 41	47.245504	13.2533426	s	259	21
Locality 41	47.245388	13.2534186	s	21	10
Locality 41	47.245355	13.2534291	axpl3	11	19
Locality 41	47.24534	13.2534249	fa2	109	4
Locality 42	47.246781	13.2544663	s	12	20
Locality 42	47.246775	13.2544657	l1	280	22
Locality 42	47.246776	13.2544675	l1	277	10
Locality 43	47.240913	13.2711432	s	48	30
Locality 43	47.248821	13.2705873	s	309	10
Locality 43	47.248826	13.2706056	s	2	28
Locality 43	47.248833	13.2706203	s	353	13
Locality 43	47.251604	13.2507555	s	21	33
Locality 43	47.240898	13.271176	l1	125	18
Locality 43	47.251605	13.2507568	l1	304	3
Locality 44	47.241327	13.2615143	s	18	26
Locality 44	47.241576	13.2675852	s	149	14
Locality 44	47.241332	13.2615303	l1	9	21
Locality 44	47.241605	13.2676356	l1	133	0
Locality 45	47.242404	13.2590995	s	349	46
Locality 45	47.242407	13.2591025	s	358	33
Locality 45	47.242444	13.2599685	Fault	154	52
Locality 45	47.242444	13.2599696	Fault	149	48
Locality 45	47.267988	13.2191994	l1	285	1
Locality 45	47.242443	13.2599777	Slickenside	83	27
Locality 45	47.24244	13.2599798	Slickenside	99	38
Locality 46	47.251866	13.1157069	s	191	62
Locality 46	47.251866	13.1157069	axpl3	280	17
Locality 46	47.251866	13.1157069	l1	282	16
Locality 46	47.251866	13.1157069	fa3	285	15
Locality 47	47.251866	13.1157069	axpl2	323	71
Locality 47	47.251866	13.1157069	axpl2	248	83
Locality 47	47.251866	13.1157069	axpl3	201	10
Locality 47	47.251866	13.1157069	fa2	293	15

Locality 47	47.251866	13.1157069	fa3	290	8
Locality 48	47.262459	13.1201986	s	292	31
Locality 48	47.262458	13.1202016	l1	272	35
Locality 49	47.265327	13.1168639	axpl2	337	76
Locality 50	47.266813	13.1160501	s	253	40
Locality 50	47.266801	13.1160404	s	278	41
Locality 50	47.266803	13.1160205	s	283	55
Locality 50	47.266795	13.1160124	s	298	60
Locality 50	47.266798	13.1160501	l1	293	15
Locality 50	47.266792	13.1160422	l1	295	14
Locality 51	47.257074	13.1335053	axpl2	14	50
Locality 51	47.257113	13.1335293	axpl3	6	4
Locality 51	47.257054	13.1335093	fa2	97	5
Locality 51	47.257111	13.1335258	fa3	104	1
Locality 52	47.255877	13.1339974	s	337	75
Locality 52	47.255902	13.1339138	s	336	81
Locality 52	47.255899	13.1339177	s	351	83
Locality 52	47.255863	13.1339645	s	292	88
Locality 52	47.255976	13.1338334	axpl3	228	31
Locality 52	47.255942	13.133855	axpl3	249	14
Locality 52	47.255939	13.1338408	s	202	47
Locality 52	47.255928	13.133802	axpl2	19	42
Locality 52	47.255918	13.1338191	axpl2	16	53
Locality 52	47.25585	13.1340237	l1	281	15
Locality 52	47.255895	13.1339746	l1	265	10
Locality 52	47.255892	13.1339752	l1	271	14
Locality 52	47.255892	13.1339546	l1	263	8
Locality 52	47.255954	13.1338348	l1	284	21
Locality 52	47.255951	13.1338394	fa3	281	12
Locality 52	47.255913	13.1338491	fa2	289	11
Locality 53	47.256193	13.1330552	axpl2	9	63
Locality 53	47.255678	13.1347612	s	332	16
Locality 53	47.255714	13.1347549	s	315	7
Locality 54	47.257107	13.131489	shearband	109	34
Locality 54	47.257181	13.1313464	axpl3	200	8
Locality 54	47.2553	13.1319929	s	192	85
Locality 54	47.256592	13.1325078	axpl3	38	14
Locality 54	47.256592	13.1325517	shearband	101	37
Locality 54	47.256548	13.1324674	shearband	103	33
Locality 54	47.257152	13.1313424	fa3	297	8
Locality 54	47.255346	13.1320694	l1	85	8
Locality 54	47.256576	13.1325508	fa3	112	13
Locality 55	47.255734	13.1303814	axpl3	357	3
Locality 55	47.255733	13.1303763	axpl2	21	40
Locality 55	47.255734	13.1303653	fa2	88	2

Locality 55	47.255736	13.1303854	fa3	111	4
Locality 56	47.238582	13.1934784	s	328	78
Locality 56	47.238582	13.1934784	l1	204	19
Locality 57	47.238582	13.1934784	s	12	35
Locality 57	47.238582	13.1934784	s	229	68
Locality 57	47.238582	13.1934784	s	207	77
Locality 57	47.238582	13.1934784	l1	298	2
Locality 57	47.238582	13.1934784	l1	140	5
Locality 58	47.238582	13.1934784	l1	101	5
Locality 58	47.245454	13.2180084	s	20	45
Locality 58	47.238582	13.1934784	shearband	105	34
Locality 58	47.238582	13.1934784	shearband	162	34
Locality 58	47.238582	13.1934784	s	13	9
135_1	47.250829	13.221651	s	10	50
135_2	47.250829	13.221651	l1	297	8
G42_1	47.242332	13.210066	s	57	42
G42_2	47.242332	13.210066	l1	260	6
G43_1	47.246519	13.213148	s	319	25
G43_2	47.246519	13.213148	l1	270	16
G44_1	47.246023	13.215729	s	340	57
G44_2	47.246023	13.215729	l1	286	44
G45_1	47.247148	13.216765	s	296	26
G45_2	47.247148	13.216765	l1	279	25
G46_1	47.246766	13.220108	s	306	12
G46_2	47.246766	13.220108	l1	278	11
G47_1	47.249475	13.220233	s	205	67
G47_2	47.249475	13.220233	l1	109	2
G48_1	47.250792	13.221928	s	28	81
G48_2	47.250792	13.221928	l1	107	1
G49_1	47.253782	13.224663	s	95	2
G49_2	47.253782	13.224663	l1	95	2
G52_1	47.255343	13.231188	s	193	85
G52_2	47.255343	13.231188	l1	102	2
G52_3	47.255343	13.231188	axpl2	19	71
G92_1	47.221527	13.278496	s	322	39
G92_2	47.221527	13.278496	l1	273	35
G92_3	47.221527	13.278496	s	342	18
G92_4	47.221527	13.278496	l1	288	12
G93_1	47.225864	13.274201	s	152	35
G93_2	47.225864	13.274201	l1	115	28
G94_1	47.231838	13.27066	s	270	1
G94_2	47.231838	13.27066	l1	290	3
G96_1	47.229933	13.273052	s	90	2
G96_2	47.229933	13.273052	l1	90	2
G96_3	47.229933	13.273052	fa3	90	2

G97_1	47.232235	13.272481	s	302	75
T101_1	47.24116	13.244642	s	11	83
T101_2	47.24116	13.244642	fa2	290	12
T101_3	47.24116	13.244642	axpl2	10	76
T101_4	47.24116	13.244642	fa3	290	18
T101_5	47.24116	13.244642	axpl3	232	13
T101_6	47.24116	13.244642	shearband	93	19
T102_1	47.244913	13.239139	s	3	23
T102_2	47.244913	13.239139	l1	297	7
T102_4	47.244913	13.239139	Fault	300	56
T102_5	47.244913	13.239139	Fault	106	56
T104_1	47.243611	13.244704	s	15	41
T104_2	47.243611	13.244704	l1	275	4
T105_1	47.244531	13.24625	s	349	21
T105_2	47.244531	13.24625	l1	320	5
T106_1	47.245103	13.247589	s	185	39
T106_2	47.245103	13.247589	l1	276	1
T106_3	47.245103	13.247589	axpl3	160	27
T106_4	47.245103	13.247589	fa3	276	1
T107_1	47.245255	13.247929	s	3	46
T109_1	47.245595	13.24937	s	90	3
T109_2	47.245595	13.24937	l1	107	1
T110_1	47.244184	13.253026	s	356	11
T110_2	47.244184	13.253026	l1	285	5
T112_1	47.245062	13.253848	s	140	19
T112_2	47.245062	13.253848	l1	112	14
T113_1	47.245454	13.253321	s	255	6
T113_2	47.245454	13.253321	l1	290	3
T113_3	47.245454	13.253321	axpl3	5	32
T114_1	47.246782	13.254492	s	121	11
T114_2	47.246782	13.254492	l1	117	8
T115_1	47.251638	13.250774	s	348	35
T115_2	47.251638	13.250774	l1	281	3
T116_1	47.24976	13.260221	s	352	67
T116_2	47.24976	13.260221	l1	279	3
T117_1	47.24886	13.268604	s	7	62
T118_1	47.248825	13.270604	s	315	14
T118_2	47.248825	13.270604	l1	279	10
T119_1	47.240863	13.271181	s	23	25
T119_2	47.240863	13.271181	l1	101	7
T120_1	47.241702	13.267671	s	283	17
T120_2	47.241702	13.267671	l1	300	16
T121_1	47.241384	13.261503	s	342	22
T121_2	47.241384	13.261503	l1	85	15
T122_1	47.242402	13.25991	s	144	46

T122_2	47.242402	13.25991	l1	90	30
T122_3	47.242402	13.25991	fa2	102	2
T131_1	47.24715	13.21326	s	209	79
T131_2	47.24715	13.21326	l1	300	9
T131_3	47.24715	13.21326	fa2	300	6
T131_4	47.24715	13.21326	axpl3	225	29
T131_5	47.24715	13.21326	shearband	113	11
T132_1	47.251446	13.22004	s	195	85
T132_2	47.251446	13.22004	l1	286	5
T132_3	47.251446	13.22004	shearband	1	71
T133_1	47.250839	13.222938	s	201	46
T134_1	47.250926	13.22167	s	210	73
T134_2	47.250926	13.22167	l1	126	4
T135_1	47.244927	13.218879	s	9	11
T135_2	47.244927	13.218879	l1	285	3
T135_3	47.244927	13.218879	shearband	114	33
T136_1	47.245389	13.217992	s	15	32
T136_2	47.245389	13.217992	l1	291	7

9.2 RSCM data after Lünsdorf et al., 2017

Sample	RSCM Thermometry after Lünsdorf et al. 2017														
	Temp [°C]	+/-	N	D_ STA	std	G_STA	std	G_ Shape factor	std	Dmax _pos	std	Gmax _pos	std	Dmax/ Gmax-ratio	std
TW12-23	370	30	20	79.7	12.8	136.4	26.8	1.8	0.3	1346.7	2.8	1585.2	5.3	1.8	0.3
TW01-24	383	30	20	76.7	7.3	96.4	20.0	2.3	0.5	1349.1	1.7	1582.4	1.7	1.4	0.2
TW02-24	351	30	20	88.8	12.1	146.8	16.2	1.7	0.3	1346.2	3.7	1587.5	4.9	1.7	0.2